Chapter 9
The Antares Explosion Observed by the USArray: An Unprecedented Collection of Infrasound Phases Recorded from the Same Event

Julien Vergoz, Alexis Le Pichon and Christophe Millet

Abstract On October 28, 2014, the launch of the Antares 130 rocket failed just after liftoff from Wallops Flight Facility, Virginia. In addition to one infrasound station of the International Monitoring Network (IMS), the explosion was largely recorded by the Transportable USArray (TA) up to distances of 1000 km. Overall, 180 infrasound arrivals were identified as tropospheric, stratospheric or thermospheric phases on 74 low-frequency sensors of the TA. The range of celerity for those phases is exceptionally broad, from 360 m/s for some tropospheric arrivals, down to 160 m/s for some thermospheric arrivals. Ray tracing simulations provide a consistent description of infrasound propagation. Using phase-dependent propagation tables, the source location is found 2 km east of ground truth information with a difference in origin time of 2 s. The detection capability of the TA at the time of the event is quantified using a frequency-dependent semiempirical attenuation. By accounting for geometrical spreading and dissipation, an accurate picture of the ground return footprint of stratospheric arrivals as well as the wave attenuation are recovered. The high-quality data and unprecedented amount and variety of observed infrasound phases represents a unique dataset for statistically evaluating atmospheric models, numerical propagation modeling, and localization methods which are used as effective verification tools for the nuclear explosion monitoring regime.

9.1 Introduction

On October 28, 2014 at 22:22:42 UTC, the launch of an Antares 130 rocket failed just after liftoff from Wallops Flight Facility, Virginia, at location 37.83 N, 75.49 W. A small explosion occurred at the bottom of the rocket 7 s after the vehicle cleared the

J. Vergoz (✉) · A. Le Pichon · C. Millet
CEA, DAM, DIF, F-91297 Arpajon, France
e-mail: julien.vergoz@cea.fr

A. Le Pichon et al. (eds.), *Infrasound Monitoring for Atmospheric Studies*,
https://doi.org/10.1007/978-3-319-75140-5_9

tower, and it fell back down onto the pad. The Range Safety officer sent the destruct command just before ground impact, creating a huge explosion 21 s after liftoff at 22:23:03 UTC (Pulli and Kofford 2015). The cause of the incident is still officially unknown and would be due to a failure of the first stage engine (NASA 2015).

Three different types of acoustic sources successively emitted infrasound signals (Pulli and Kofford 2015): (1) first stage ignition and rocket liftoff during the first 7 s of ascendant flight at subsonic velocity (Lighthill 1963; Varnier 2001), (2) the small explosion occurring at the bottom of the rocket associated to the incident, and (3) the rocket explosion caused by the destruct command. The latter source is massive and unquestionably the most energetic. It is the only one that has been captured by remote stations, at distances larger than 100 km. These three sources have been observed at 57 km, where the measured amplitudes and frequency content provide detailed information about their energy (Pulli and Kofford 2015).

With an average inter-station spacing of ~2000 km, the sparse spatial sampling of the acoustic wave field by the International Monitoring System (IMS) (Marty 2019) infrasound network does not allow precise propagation studies, especially at regional distances. The benefits of augmenting the spatial coverage of the IMS network to provide a detailed picture of acoustic wave propagation has been demonstrated by number of studies (Green et al. 2009; Edwards et al. 2014; Gibbons et al. 2015; Che et al. 2017; de Groot-Hedlin and Hedlin 2019). For the large-scale Sayarim calibration experiments (on August 26, 2009 and January 26, 2011), the temporary deployed array stations at regional and telesonic distances measured a unique collection of high amplitude infrasound phases (tropospheric, stratospheric and thermospheric) and allowed specific propagation effects to be highlighted that IMS stations could not capture (Fee et al. 2013; Waxler and Assink 2019). For the Antares explosion, only one infrasound station of the IMS network (I51GB, in Bermuda) recorded multiple arrivals from the event at about 1100 km.

With an inter-station spacing of about 70 km, the Transportable USArray (TA) provides a unique set of high temporal frequency surface atmospheric pressure observations at a continental scale. It consists of approximately 400 seismo-acoustic stations primarily deployed for seismic measurements. This dense measurement platform offers opportunities for detecting and locating geophysical events (Walker et al. 2011; De Groot-Hedlin and Hedlin 2015; de Groot-Hedlin and Hedlin 2019) and reveals large acoustic events that may provide useful insight into the nature of long-range infrasound propagation in the atmosphere (De Groot-Hedlin and Hedlin 2014; Assink et al. 2019). At the time of the event, the TA was located close to the east coast of the United States and surrounded the explosion. 226 operating stations were located at less than 2000 km from the event and all were equipped with single infrasound microphones.

In this chapter, we present a detailed analysis of infrasound recordings generated by the explosion of the Antares rocket associated to its destruction. This event is

among the most interesting, recent explosive sources representing a unique dataset for statistically evaluating atmospheric models, numerical propagation modeling and localization methods. Section 9.2 presents the observation network, the recording conditions influenced both by the surface background noise level and the general circulation of the atmosphere from the ground to the lower thermosphere, and an overview of near and far-field infrasound recordings. Section 9.3 presents both ray tracing simulations and source location results. It is shown that phase identification is made without ambiguity so that location results obtained with and without phase-dependent travel time curves can be compared. The frequency-dependent attenuation of stratospheric phases is studied as a function of the effective sound speed in Sect. 9.4. Observations and simulation results are discussed in the last Section.

9.2 Observations Network and Recordings Conditions

9.2.1 Observation Network

The TA consists of 400 high-quality broadband seismographs and atmospheric sensors that have been operated at temporary sites across the United States from West to East in a regular grid pattern. In August 2007, the first footprint was established from North to South along the westernmost quarter of the United States. The TA finished its eastward migration in fall 2013, just before the Antares accident, and is still deployed in Alaska in June 2017. The inter-station distance is about 70 km; such a dense network is very useful for studying regional infrasound propagation and studying middle atmospheric dynamics (de Groot-Hedlin and Hedlin 2019). Data from each station are continuously transmitted to the Array Network Facility at the University of California, San Diego, where initial operational and quality checks are performed, and then sent to the Incorporated Research Institutions for Seismology (IRIS) Data Management Center (https://www.iris.edu), where all data and associated metadata are archived.

Infrasound sensors are single Hyperion microphones with a flat response between 0.01 and 20 Hz (Merchant 2015). They are not connected to a wind noise reducing system (Raspet et al. 2019). No standard array processing method, as used at the International Data Center (IDC) to process IMS infrasound network data (Mialle et al. 2019), can be applied to identify the arrivals recorded by the TA. As a consequence, the exploitation of such a network for infrasound propagation and atmospheric studies requires quiet meteorological conditions for an unambiguous discrimination between infrasound arrivals and wind bursts.

Among the 400 stations, 226 were operational and located at less than 2000 km from the launch pad at the time of the Antares event. A large high-pressure system was centered off the Eastern USA shore and at liftoff time (22:22:42 UTC),

the night has just fallen so that atmospheric turbulence reduced and night breezes have not yet risen on the coast. Thanks to those stable atmospheric conditions in the boundary layer, most of the stations of the TA exhibited low acoustic background noise before the accident, as shown in Fig. 9.1. Background noise levels are Root Mean Squared (RMS) values calculated in the 0.05–0.5 Hz frequency band for 20 min time windows, just before the fastest arrivals (set to 360 m/s at all stations, see Sect. 2.4). In this frequency band, the RMS amplitude calculated at all station is a good proxy to assess local wind noise conditions (Alcoverro and Le Pichon 2005; Walker and Hedlin 2009). This measure provides an estimate of the capability of the station to detect a broadband or low-frequency signal, such as thermospheric waves. Background colors are absolute wind speeds derived from zonal and meridional wind speeds of the first level of the ECMWF operational products (https://www.ecmwf.int/) at 21:00 UTC. At most stations, the synoptic wind speed does not exceed 3 m/s. 60% of the stations exhibit RMS amplitudes lower than 0. 1 Pa RMS, with lowest values reached in the northeast and southwest quadrants. Following this procedure, 180 identified phases at 74 stations (shown in Fig. 9.1) have been picked at the quietest stations (blue), except for the closest stations, where amplitudes are large enough to be picked whatever wind noise. In particular,

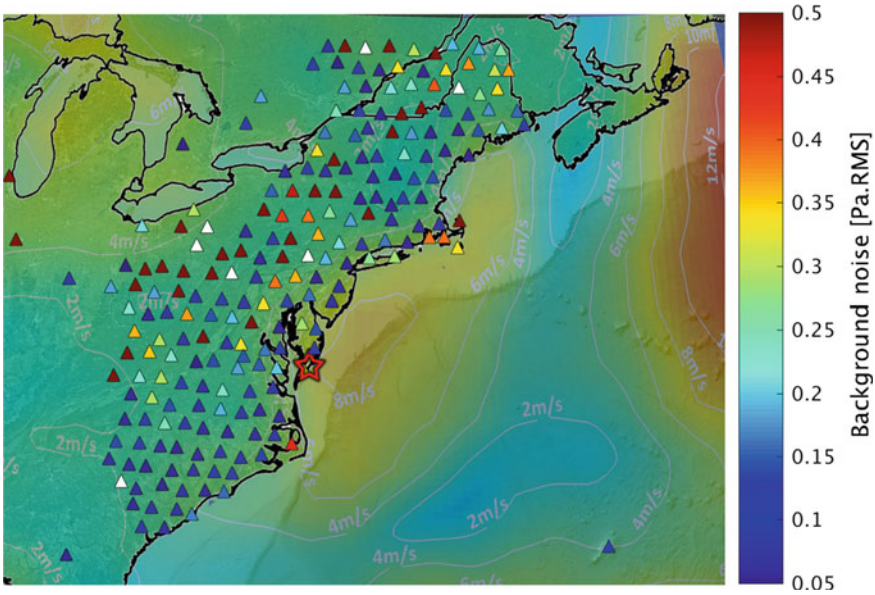

Fig. 9.1 Status of the transportable USArray at the time of Antares accident. Red star is the rocket launch pad location, triangles are stations with colors referring to acoustic background noise just before liftoff. White triangles are stations without data. Background colors code wind speed values extracted from the first level of ECWMF operational analyses, at 21:00 UTC. The steady boundary layer in addition to favorable propagation conditions has allowed picking 180 infrasound arrivals that propagated in the tropospheric, stratospheric and thermospheric waveguides

all thermospheric phases (see Sect. 2.4.3) have only been recorded on dark blue stations in the southwest quadrant. This procedure allows the probability of misidentification of arrivals on single sensors to be reduced.

9.2.2 Atmospheric Specifications

Regarding propagation modeling, the temperature and wind specifications are extracted from the ECMWF operational analyses part of the Integrated Forecast System (IFS) (91 vertical levels up to 0.01 hPa with a horizontal resolution of half a degree and a temporal resolution of 3 h) from the ground to about 80 km altitude. Above 90 km, the empirical MSIS-00 (Picone et al. 2002) and HWM-07 (Drob et al. 2008) models are used for temperature and wind speed, respectively. A cubic spline curve fitting approach is applied between 80 and 90 km to connect ECMWF wind and temperature profiles with empirical models.

In Fig. 9.2, snapshots of maximum horizontal winds are plotted for three different slices of altitude, ranging from the lower troposphere to the lower mesosphere. In addition, range-dependent vertical profiles of down- and crossed winds, temperature and effective sound speed are shown for two stations located at approximately 1000 km from the event, in opposite directions: TIGA (South-West, green station) and H65A (North-East, red station). The effective sound speed represents the combined effects of refraction due to sound speed gradients and advection due to along-path wind on infrasound propagation. Color gradient shows the variability of the different parameters along the great circle paths, between the source (in black) and the two selected stations (in color).

Above the TA stations, the propagation conditions are exceptional because winds blow northeastwards from the ground level to ~80 km altitude. Such a feature is very clear in Fig. 9.2d, e showing positive down and crossed winds until 80 km for northeastwards propagation. Two main geometric ducts exist. First, a stable stratospheric duct for which the effective sound speed between 40 and 80 km is much larger than the effective sound speed at the ground level. In this range of altitude, crossed winds reach 80 m/s, which significantly deflect the wavefront from its original launch direction (Garcés et al. 1998). Second, a thin duct in the boundary layer, between the ground level and around 1 km altitude (Fig. 9.2h) was generated by a temperature inversion (more pronounced in the vicinity of the source) coupled with moderate jets (around 20 m/s). As opposed to the stratospheric duct, the tropospheric duct varies significantly in strength, so that range-dependent features are expected to be of importance for propagation simulations. The altitudes of refraction of the waves propagating in this duct are comparable to typical infrasound wavelengths (between tens of meters to more than one kilometer) so that dispersion signatures are expected to be observed for such paths (De Groot-Hedlin 2017).

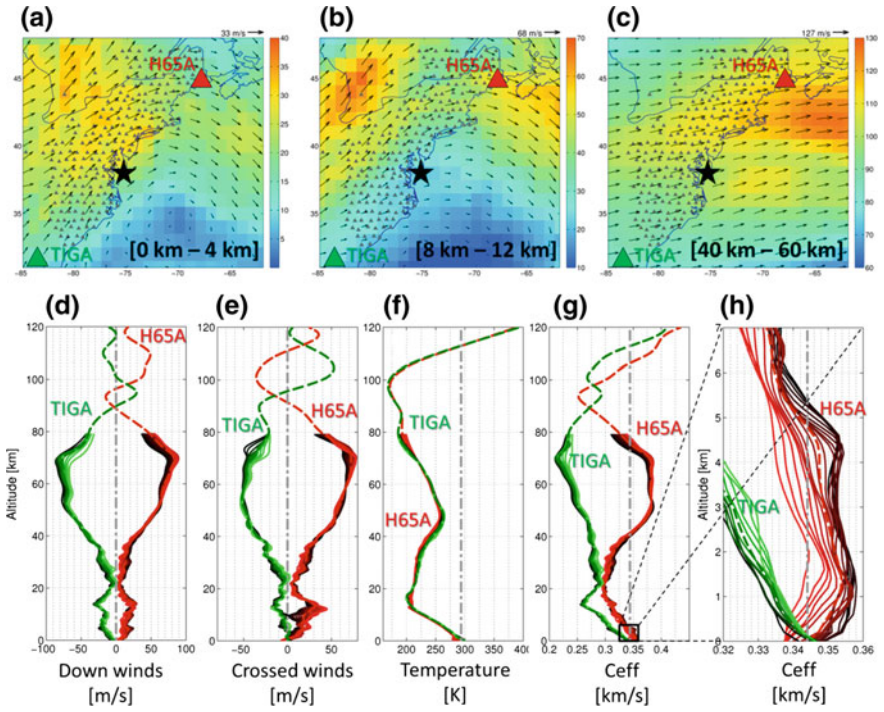

Fig. 9.2 Maps of maximum horizontal winds derived from ECMWF operational analyses in the lower troposphere (**a**), tropopause (**b**) and stratopause (**c**). At all altitudes, winds blow northeastwards. Range-dependent vertical profiles of down winds (**d**), crossed winds (**e**), temperature (**f**), effective sound speed (**g**) until 120 km and zoom of the effective sound speed until 7 km (**h**), are plotted for two stations located about 1000 km from the event, in opposite directions (H65A northeast and TIGA southwest). Color gradients show the vertical variability of the different parameters along the great circle paths, between the source (black star on the maps corresponding to the black profiles below) and the two stations (colored triangles on the maps corresponding to the colored profiles below)

9.2.3 Near-Field Measurements

When searching for infrasound arrivals generated by an event of interest, it is the routine for the analysts to focus first on the closest stations, regardless of propagation conditions. Such an approach is well suited when the spatial distribution of the stations is sparse and the number of stations is limited (e.g., the IMS infrasound network). Array processing helps to discriminate between wind gusts and coherent arrivals (Mialle et al. 2019) and to check whether arrival times and direction of arrivals are consistent with the event. Analyzing waveforms from a dense network of single sensors can also provide a detailed picture of propagation paths at a regional scale.

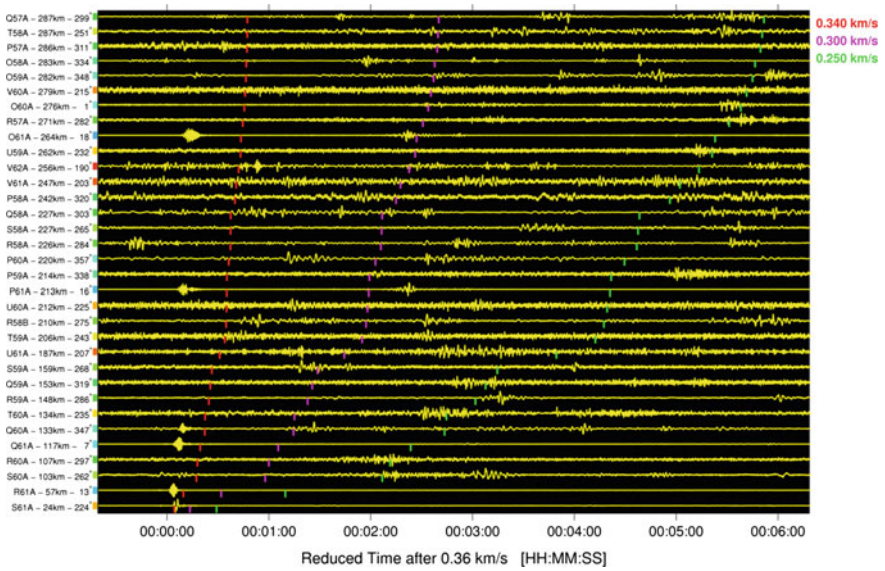

Fig. 9.3 Waveforms of the 34 closest infrasound stations located at less than 300 km from the source, sorted by distance from bottom to top. Station names, distances, and azimuths are specified to the left. A 0.5–4 Hz passband filter is applied and amplitudes are normalized. X-scale is reduced time relative to 360 m/s. Vertical red, magenta, and green vertical bars indicate, respectively 340 m/s, 300 m/s, and 250 m/s celerities so that arrivals associated to the event are typically expected to be visible between the red and green bars (Brown et al. 2012). For these stations, time windows, and filter parameters, only a few arrivals with celerities larger than 340 m/s and around 300 m/s are identified, especially to the northern part of the network

Figure 9.3 shows the waveforms from the 34 closest stations of the USArray located at distances less than 300 km from the Wallops Flight Facility. Waveforms are filtered in the 0.5–4 Hz frequency band and plotted in a time window adjusted to travel times controlled by celerities ranging from 250 to 340 m/s, typical of thermospheric and tropospheric propagation (Brown et al. 2002; Fee et al. 2013). Under strong stratospheric jets conditions, fast stratospheric arrivals (Waxler et al. 2015) can propagate with celerity as high as 360 m/s. Thermospheric waves can propagate at celerity as low as 210 m/s (Assink et al. 2012) and even significantly lower as shown in this study. For that reasons, time windows have been extended accordingly in Fig. 9.3. The vertical red, magenta, and green vertical bars indicate celerities of 340, 300, and 250 m/s, respectively. Surprisingly, no clear arrivals are identified between these bars excepted at two stations (O61A, P61A) with arrivals at around 300 m/s. Only the two closest stations S61A (24 km) and R61A (57 km) exhibit high amplitude single arrivals with different signatures (see details on Fig. 9.4). At other stations, only a few arrivals with a celerity around 360 m/s can be identified unambiguously to the North, with azimuths ranging between 347° and 16°. It is worth noting that due to the event location and the coast orientation, most

of the 34 closest stations are located West of the event, which in this situation is upwind (see Sect. 2.2).

Only two stations are located at distances less than 100 km from the event, while 32 are between 100 and 300 km. These two stations captured well the main explosion caused by rocket destruction, but also exhibit signals from the ignition and liftoff (R61A), as well as the small explosion at the bottom of the rocket (S61A, R61A). The analysis of these signals provides information about the chronology and the energy ratios of the event (Pulli and Kofford 2015).

The rocket destruction labeled as "explosion" on Fig. 9.4 is captured by the two stations with different signatures. The corresponding arrivals are manually picked as "Iw". The closest station, S61A, located 24 km southwest of the event, exhibits a symmetrical "N shape" wave with a dominant frequency of 0.4 Hz, a maximum overpressure peak of 7.6 Pa and a celerity of 342 m/s. The other station, in the opposite direction and 2.4 times farther, exhibits a clear dispersive wave train of 6 s duration with maximum energy between 0.5 and 4 Hz, a maximum amplitude of 24 Pa (more than three times larger than the one observed at the closest station) and a high celerity value of 360 m/s. As shown in Fig. 9.2h, the temperature inversion coupled with the shallow northeastwards jets cause very different propagation in opposite directions, even at short distances. The dominant frequencies observed at R61A are consistent with the duct thickness of about 1 km and the downwind advection of about 20 m/s explains the high celerity for that arrival.

This analysis illustrates how the propagation medium significantly affects waveforms even at short distances, suggesting that particular caution has to be paid when processing waveforms, especially when estimating the acoustic source energy. Existing empirical models such as those proposed by Kinney and Graham (1985) or Pierce et al. (1973) do not take into account the variability of the atmosphere (Garces 2019). Fitting the N shape wave observed at S61A with theoretical blast waves (Reed 1977) would lead to large errors: the measured positive phase duration is inconsistent with the maximum overpressure peak. To get around this problem associated to atmospheric conditions, Kim and Rodgers (2016) propose a full 3-D finite difference method that can reasonably be applied when considering propagation ranges of a few tens of kilometers.

The small explosion which occurs at the bottom of the rocket (NASA 2015; Pulli and Kofford 2015) is labelled here as "incident" and is visible at both S61A and R61A stations. Due to the favorable North Eastwards tropospheric jet, the frequency content is very different at the two stations. While most of the energy is trapped in the shallow tropospheric duct for R61A with maximum amplitudes between 0.5 Hz and 4 Hz, the signal at S61A exhibits much higher frequencies, between 8 and 20 Hz. The most energetic arrival is associated with the rocket destruction and is the only one detected at larger distances. In the following, we focus only on signals generated by this event.

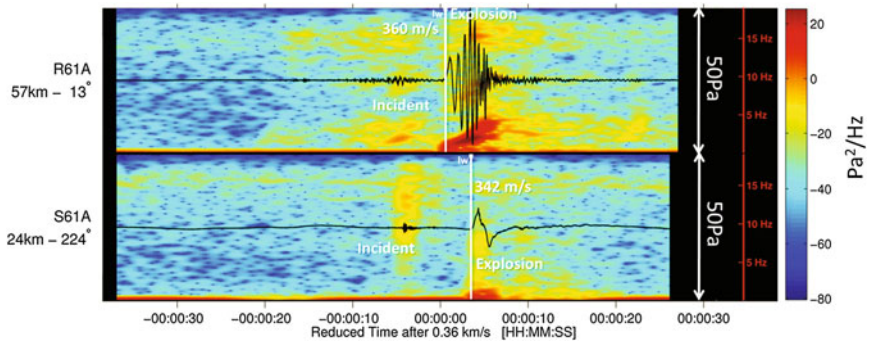

Fig. 9.4 Details on raw waveforms recorded by the two stations located at distance less than 100 km from the event (S61A, 24 km, South-West and R61A, 57 km, North-East). Spectrograms between 0.1 and 20 Hz are plotted in the background. The same amplitude and frequency vertical scales have been applied for both stations. The manually picked vertical white bars are associated to the rocket destruction event. For that latter event, the frequency content and waveform signatures are different at the two stations, with maximum amplitude more than 3 times larger at R61A, although 2.4 times farther than S61A

9.2.4 Far-Field Measurements

Signals with the largest signal-to-noise ratio (SNR) are expected in regions where the background noise is the lowest (blue stations on Fig. 9.1) along North/North-East paths (favorable tropospheric and stratospheric propagation, see Fig. 9.2). This identification strategy is more efficient than the one adopted in Sect. 2.3, where signals of interest can be drowned within incoherent noise, as shown in Fig. 9.3, on which signals are difficult to identify.

9.2.4.1 Tropospheric Phases

Overall, 27 tropospheric arrivals have been identified. 26 arrivals have been manually picked at 26 stations North-East of the event up to 1051 km, plus one at the closest station S61A located 24 km South-West of the event. Picks are represented by vertical white bars labeled as "Iw" in Fig. 9.5. All tropospheric arrivals recorded North-East have common features, which are given as follows:

(1) The celerity values are abnormally high for tropospheric arrivals (between 360 m/s for the closest stations and 350 m/s for the farthest stations) while typical values are expected around the speed of sound at the ground level (i.e., 340 m/s). This feature is explained by the moderate northeastwards advection

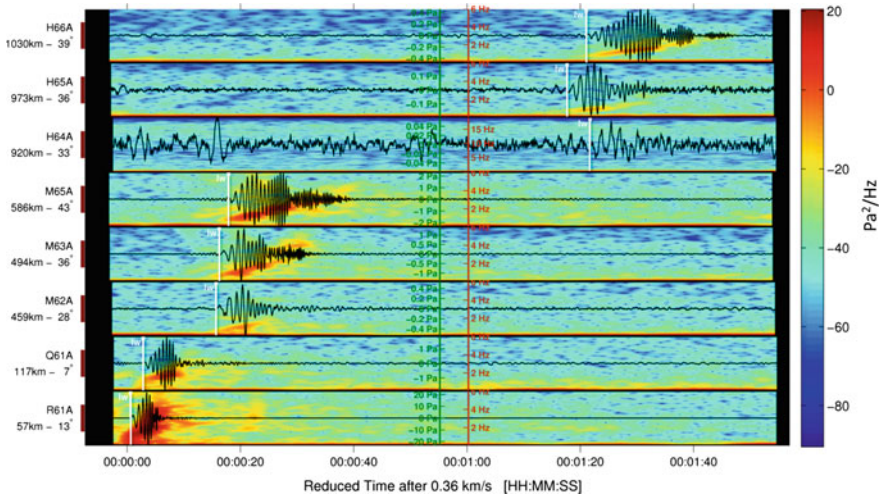

Fig. 9.5 Example of tropospheric dispersive waves at distances ranging from 57 to 1030 km in the North-East direction. Station names, distances, and azimuths are specified to the left. A 0.5–4 Hz passband filter is applied and amplitudes are normalized by station. X-scale is reduced time relative to 360 m/s. Spectrograms between 0.1 and 6 Hz are plotted in the background. While waveforms are different in shapes, amplitudes, and durations, they exhibit similar dispersion patterns

in lower troposphere (around 20 m/s) which persists along the North-East coastline.

(2) The frequency contents are comparable, between 0.5 and 4 Hz, with pronounced dispersion patterns increasing with distance. The most striking dispersion curves are shown in Fig. 9.5. This feature is explained by the shallowness of the tropospheric duct. When the thickness of the waveguide is comparable to the signal wavelength (maximum refracting height of ~1 km altitude), dispersion occurs (Waxler 2003; Talmadge et al. 2008). It is worth noting that waveforms vary significantly in shape, amplitude, and duration from one station to another depending on the structure of the waveguide.

(3) The amplitudes of the tropospheric waves strongly depend on the direction of propagation, as it can be observed when comparing signals at M62A, M63A, and M65A to signals at H64A, H65A, and H66A. These differences are explained by two effects: (1) the shallow tropospheric duct slightly weakens with more northernly propagation; (2) the propagation to the easternmost stations occurs above the ocean. For example, the propagation path to H66A, located 1030 km North-East (39°) of the event is almost purely oceanic and the maximum amplitude is 0.5 Pa. For H65A (973 km, 36°) and H64A (920 km, 33°), the amplitude drops down to 0.15 and 0.05 Pa, respectively. Within these

ducts, the atmospheric attenuation is comparable, only ground/topography interactions change. The same behavior is observed at M62A, M63A, and M65A. Full waveform modeling accounting for ground impedance and topography could explain this effect (e.g., Waxler and Assink 2019; de Groot-Hedlin and Hedlin 2019).

9.2.4.2 Stratospheric Phases

Following the same methodology, a large amount of stratospheric phases have been manually identified and picked at distances between 197 km (P61A) and 1154 km (I51 GB). Stations, where stratospheric arrivals are picked, are located in a narrow range of azimuths (except for the I51 GB IMS station), revealing the footprint of stratospheric branches thanks to the high density of stations. 107 stratospheric arrivals are labeled from Is1 to Is7, with celerities ranging from 270 to 340 m/s.

Figure 9.6 shows the waveforms of the 14 quietest stations located North-East of the event (most stations are located in directions between 26° and 36°), from 57 km (R61A) to 973 km (H65A). Unlike Fig. 9.3, phase picking and labeling is straight-forward: the fastest arrivals are tropospheric waves and are recognized from their pronounced dispersive patterns (see previous section). Then, the first visible stratospheric bounce occurs at 213 km (Q61A), second bounce at 386 km (N62A), third bounce at 636 km (K63A), fourth bounce at 804 km (I63A), and fifth bounce at 920 km (H64A). Phase labeling is made without any ambiguity at stations with high SNR values (like those of Fig. 9.6) and are compared to other nearby stations for which the identification is trickier.

Is1 is still observed at more than 1000 km with a celerity of 340 m/s, which is typical for tropospheric arrivals. Fast stratospheric arrivals have already been observed in the literature (Evers and Haak 2007), however, they do not belong to the fast branch as identified by Waxler et al. (2015). For this event, all picked stratospheric arrivals have arrival times consistent with propagation at shallow incidence angles, as confirmed by ray tracing simulations (see Sect. 9.3). Such observation is original and occurs because of the uncommon atmospheric state where moderate to strong winds blow in a North-East direction at all altitudes from ground to lower mesosphere (Fig. 9.2d, red curves). North-East advection here plays a major role in controlling the propagation times of both tropospheric and stratospheric phases.

However, a few stratospheric arrivals have much smaller celerity values, between 270 and 290 m/s. Such arrivals are only observed at quiet northern stations with azimuth ranging from 356° to 15° (J57A, J58A, J59A). The frequency content and waveform amplitudes at those stations are lower than at other stations and correspond to effective sound speed ratios (dimensionless parameter defined by the

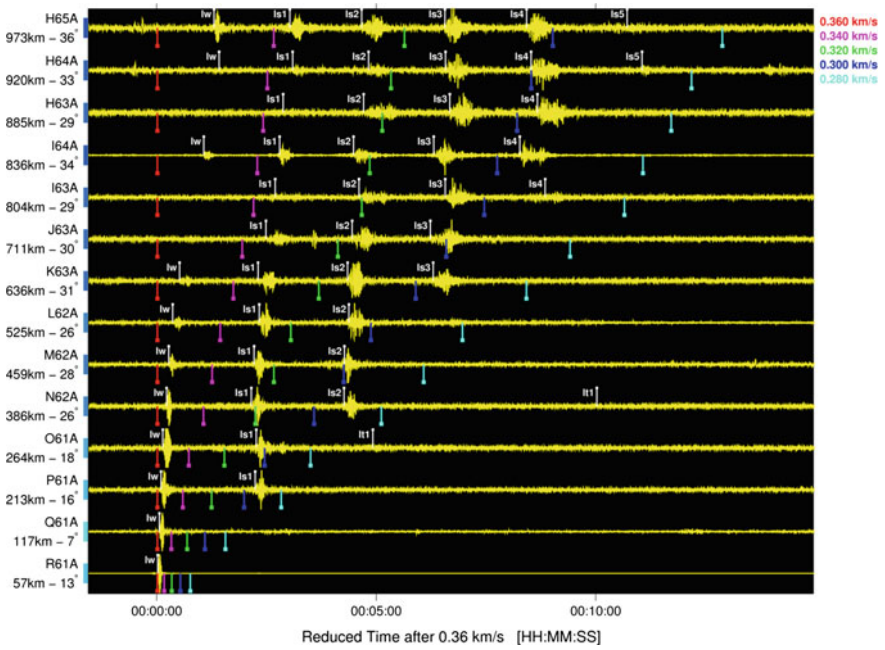

Fig. 9.6 Example of tropospheric and stratospheric returns at North-East stations from 57 to 973 km, sorted by distance from bottom to top. Station names, distances, and azimuths are specified to the left. A 0.5–4 Hz passband filter is applied and amplitudes are normalized by station. X-scale is reduced time relative to 360 m/s. The vertical white bars, manually picked as Iw and Is phases, are associated to the rocket destruction. Such a representation allows identifying unambiguously stratospheric branches from Is1 (which persists from 213 to 1000 km) to Is5 (which appears at 920 km). These branches are consistent with the so-called "slow stratospheric branches" (see Sect. 9.3) and are unusually fast for such typical stratospheric branches (Is1 celerity is 340 m/s at 973 km). The vertical colored bars indicate celerities from 360 m/s (red) to 280 m/s (cyan)

ratio between the effective sound speed at 50 km altitude and the sound speed at the ground level) slightly lower than 1. Arrival shapes are more emergent and last longer compared with stations, where the effective sound speed is larger than 1. These diffracted arrivals (depicted as "Is diff" on Fig. 9.9) observed upwind were reported by Green et al. (2011).

9.2.4.3 Thermospheric Phases

In the downwind direction, the increase of the effective sound speed with altitude refracts infrasound back to the ground surface. In contrast, when acoustic propagation occurs upwind, the decrease of the effective sound speed refracts infrasound upwards. The ground-to-stratosphere acoustic waveguide is less likely to exist, increasing the likelihood that the sound will propagate toward the thermosphere.

The decrease of density in the mesosphere and lower thermosphere controls the wave attenuation, the effects of which are especially pronounced at high frequencies. While vibrational losses are the main process of absorption in the middle atmosphere (up to 60 km at 0.5 Hz), classical and rotational relaxation losses dominate above ~80 km altitude (Sutherland and Bass 2004). Moreover, at such altitudes, signal amplitude increases due to the reduction in density. The high amplitude compressional phases are 'hot' and therefore travel faster, while the high amplitude rarefaction phases are 'cold' and therefore travel slower. Hence the signal lengthens as the compressional and rarefaction phases move at different speeds (e.g. Pierce et al. 1973, Gainville et al. 2009; Sabatini et al. 2016). The signal duration and dominant frequency are essentially controlled by the source energy and the turning height of the waves (Waxler and Assink 2019). Consequently, the dominant frequency of the thermospheric returns is expected to be lower than other tropospheric and stratospheric phases.

By lowering the frequency band, the SNR decreases as the background noise is more sensitive to atmospheric turbulences and wind bursts (Walker and Hedlin 2009). Because thermospheric returns are predicted in all directions due to the strong increase of the temperature in the lower thermosphere, focus is given to the stations which exhibit the lowest background noise (i.e., dark blue stations in Fig. 9.1), without preferred directions.

46 thermospheric phases have been picked and identified mostly on stations located South-West from 187 km (U61A) to 1026 km (TIGA). Following the same strategy applied for stratospheric arrivals, It1 to It4 phases have been identified. Figure 9.7 presents the waveforms at 30 stations, where 46 arrivals have been picked. Due to the strong attenuation of these phases, their observations are often limited to the first thermospheric bounce for energetic events (e.g., Ceranna et al. 2009). As was done for stratospheric arrivals, visualizing waveforms in a reduced time plot (Fig. 9.7) allows consecutive branches to be identified, and phases are labelled without ambiguity. The number of picked thermospheric phases is unprecedented. Ray tracing simulations (Fig. 9.13) and arrival alignments in range-celerity plots (Fig. 9.9) provide results consistent with these observations. A brute force identification of low SNR phases, trace by trace, without selecting station considering their background noise levels would have been probably impossible.

The following thermospheric returns exhibit unusual features:

(1) Celerities of most arrivals are exceptionally low. Among the 44 picked arrivals, 35 have celerities between 160 and 220 m/s. The first It2 pick at V59A (at 336 km) and It3 pick at W57A (at 501 km) have celerities of 160 m/s, which is significantly low compared with values found in the literature. So far, only Assink et al. (2012) reported celerities of 220 m/s at the first thermospheric bounce from volcano eruptions. Due to the northeastwards tropospheric flow, tropospheric phases propagate as high as 360 m/s (Sect. 2.4.1) and a few stratospheric phases propagate at 340 m/s (Sect. 2.4.2). In the opposite direction, the propagation is upwind (Fig. 9.2d, green curves) at all altitudes so that advection reduces wave celerities.

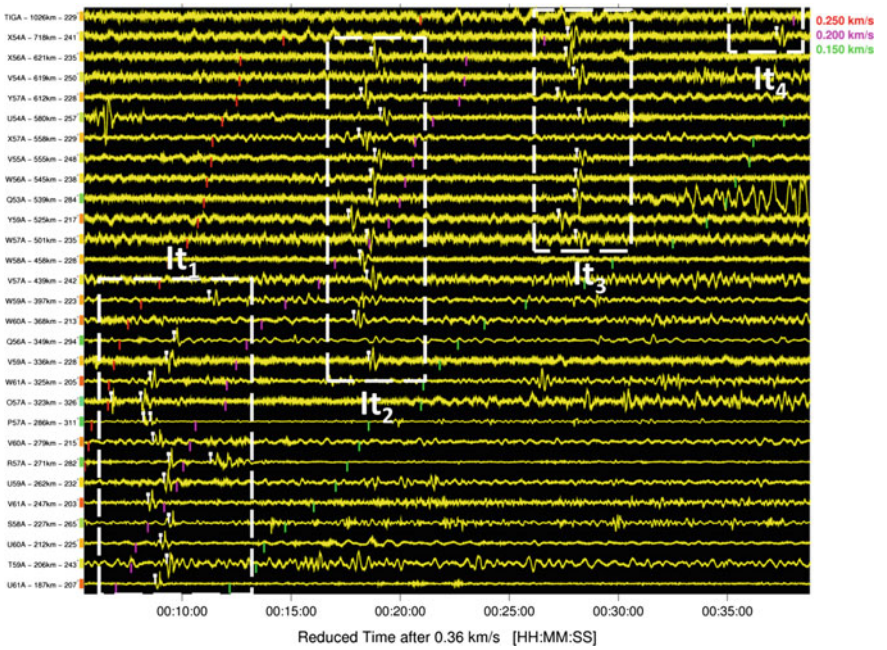

Fig. 9.7 Waveforms at the 29 quietest stations of the South-West quadrant, from 187 km (U61A) to 1026 km (TIGA), sorted by distance from bottom to top. X-scale is reduced time relative to 360 m/s. Station names, distances, and azimuths are specified to the left. A broad 0.05–10 Hz passband filter is applied to capture low frequencies and shocks. Amplitudes are normalized by station. 44 thermospheric returns are manually picked. The vertical white bars are manual It picks associated to rocket destruction. Such a representation allows the identification of unambiguously thermospheric branches from It1 (beyond 187 km) to It4 (beyond 718 km). Exceptionally low celerities are associated to the first It2 and It3 arrivals, which are as low as 160 m/s. The vertical colored bars indicate celerities from 250 m/s (red) down to 150 m/s (green)

(2) Bounces occur at short distances from the source. For example, the first thermospheric bounce is observed at 187 km. This is unusual for the thermospheric return which generally occurs between 200 and 300 km.
(3) While It3 and It4 arrivals are stable in shape and duration, the arrivals at the first thermospheric bounce exhibit very different signatures (see Fig. 9.8). Depending on the distance and the direction, the results of nonlinear effects and absorption in the mesosphere and lower mesosphere combined with additional caustic effects cause, some It1 phases to exhibit typical "N" shape shocks while others exhibit smoothed "U" shapes, or a simple sine arch. This collection of shapes provides useful information on both propagation medium (turning height) and source energy (from arrival duration).

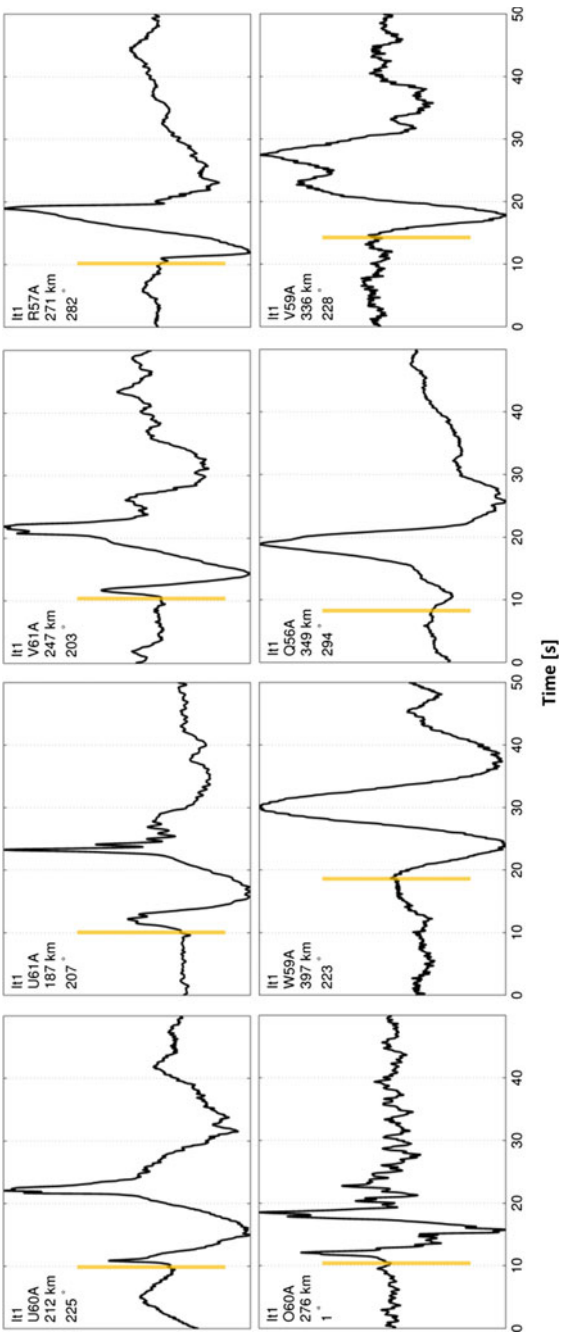

Fig. 9.8 Representative signatures of thermospheric phases at the first bounce. Station names, distances, and azimuths are specified in the top left corner of each panel. Depending on the distance and the direction, some It1 phases exhibits typical "N" wave (Q56A, R57A), shocked "U" (U60A, U61A, O60A) and smoothed "U" waves (W59A) or a simple sine arch wave (It2 → It4, not plotted here). The vertical orange bars are manual It1 picks

9.2.4.4 Observations Summary

Such a dense measurement platform offers good opportunities to provide detailed insight into propagation features at regional and continental scales (Walker et al. 2011; De Groot-Hedlin and Hedlin 2015), even when conventional array processing methods such as PMCC (Progressive Multi-Channel Correlation, Cansi 1995) or F-detector (Smart and Flinn 1971) cannot be applied. The amount and variety of infrasound arrivals observed for this event are uncommon with 180 manual picks identified as tropospheric, stratospheric or thermospheric arrivals at 74 stations of the TA. The dense spatial coverage of the TA and high SNRs allow clear and unambiguous phase identification. The exceptional range of arrival celerities, ranging from 360 m/s for tropospheric phases down to 160 m/s for thermospheric phases is the most striking result.

Figure 9.9a shows the spatial distribution of the different phases detected. Figure 9.9b shows all picks in a classical celerity-range diagram, useful for identify propagation branches. A blind identification and phase labeling have been done without simulation (e.g., ray tracing, see Sect. 9.3). The different tropospheric, stratospheric, and thermospheric branches are identified in waveform plots, considering the quietest stations, appropriate filter parameters, and time windows.

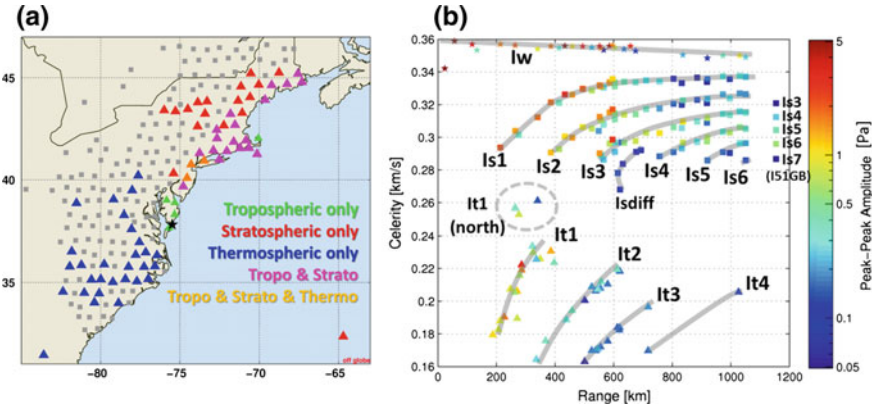

Fig. 9.9 **a** Spatial distribution of detecting stations. Colors indicate phase types. Green stations detect only tropospheric arrivals, red stations detect only stratospheric arrivals, blue stations detect only thermospheric arrivals, magenta stations detect both tropospheric and stratospheric arrivals, and orange stations detect tropospheric, stratospheric and thermospheric arrivals. The atmospheric state at the time of the event together with event location, coast orientation, and station distribution explain the South-West/North-East separation of thermospheric/tropospheric–stratospheric phases. **b** Celerity-range diagram. Colored squares and triangles represent stratospheric and thermospheric arrivals, respectively. Color codes the peak-to-peak amplitude in Pa. Iw, Is1 to Is6 and It1 to It4 branches are identified (gray lines) and show the unexpected broad range of celerities, from 360 m/s for tropospheric arrivals detected at the closest stations down to 160 m/s for some It2 and It3 thermospheric phases. The celerity of Is1 branch reaches 340 m/s at 1000 km, which is also an unusual observation

Branches of different phases are highlighted in gray in Fig. 9.9b. Iw, Is1 to Is6 and It1 to It4 branches are identified. Three main groups of arrivals do not align properly with these branches, which are given as follows:

- Five stratospheric arrivals at the IMS station I51 GB at 1154 km (Is3 to Is7) cannot be labeled without simulation (see Fig. 9.10 in the next section). Unlike other stratospheric arrivals which are picked North-East of the event, no stations is located to the South-East.
- Four It1 arrivals denoted as "It1 (north)" in Fig. 9.9b. These thermospheric arrivals are the only ones that have been picked to the North (N61A, N62A, O60A, and O61A), under stratospheric downwind conditions. Unlike all other picked thermospheric arrivals to the South-West, associated celerities to the North range between 245 and 260 m/s (Fig. 9.9a, orange stations).
- Five stratospheric arrivals along "Isdiff" branch. These stratospheric arrivals are the only ones which have been picked for paths where the effective sound speeds are slightly lower than 1, at the western most red stations I59A, I60A, J57A, J58A, and J59A (Fig. 9.9a). Arrivals at those stations are more diffused and exhibit lower celerities and smaller amplitudes compared to those of geometric arrivals. These arrivals are also studied in Sect. 9.4.

9.3 Phase Identification and Location

180 phases associated to the Antares event have been identified at 74 stations. From these phases, 185 measures were derived: 180 arrival times (175 at TA stations, 5 at I51 GB) and 5 back azimuths (at I51 GB). We have seen in Sect. 9.2 that extreme celerity values of most of those phases are unusual while other are more typical especially for stratospheric returns, as shown by Nippress et al. (2014) under typical summer conditions. The impact of the broad range of celerities derived from ray tracing simulations on the source location is here evaluated and compared with the location result using empirical propagation tables.

9.3.1 Construction of Propagation Tables

The first step in the location procedure is to build propagation tables in celerity and azimuthal deviation from a pre-location, by station and by phase, and to assign them to each measure. Such tables depend on the atmospheric state between the source and the stations, at the time of the event. This step requires the construction of propagation tables per phase and bounce order, and the labeling of the detected infrasound phases. Considering the various types of phases, the possibly large number of bounces and the likely rough pre-location, the probability of wrong phase identification is high and can degrade the location result when done automatically.

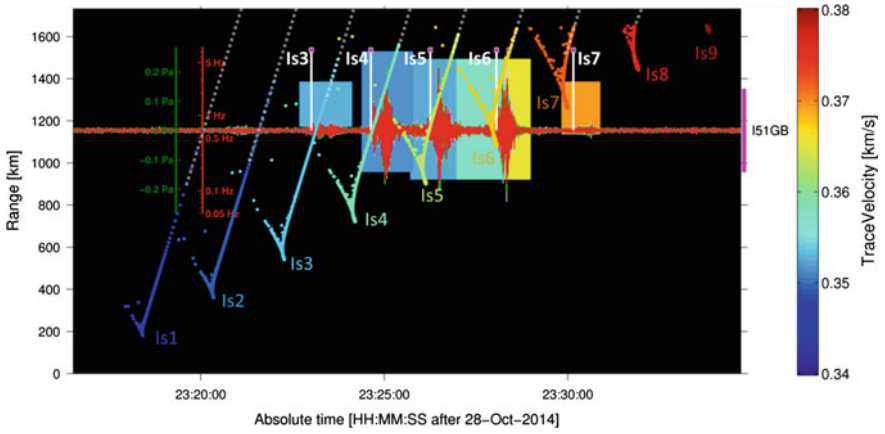

Fig. 9.10 Recorded waveforms at I51 GB, 1154 km South-East of the event. Ray bounces superimposed in the range-time space allow the identification of stratospheric arrivals, from Is3 to Is7. Colored rectangles in the background are PMCC detections in the time-frequency space with trace velocity color coded. Dashed gray lines are linear extrapolation of slow celerity stratospheric branches, referred to as "branch extension" in the next Section

In the automatic processing pipeline, phase-dependent empirical tables are generally preferred. Brown et al. (2002), Brachet et al. (2009) and Fee et al. (2013) showed that the different phases have distinct celerity ranges. Celerities have typical values of 340, 300, and 250 m/s for tropospheric, stratospheric, and thermospheric arrivals, respectively. In the case of the Antares event, celerities exhibit deviations beyond wide ranges already highlighted in several studies (Ceranna et al. 2009; Assink et al. 2012; Waxler et al. 2015). In order to quantify the location errors, location results derived from empirical tables and ray tracing simulations with phases interactively labeled are compared.

Classical ray tracing methods (e.g., Candel 1977) are often used to compute arrival time and geometrical wave characteristics needed to build propagation tables (e.g., Ceranna et al. 2009). The main reasons are given as follows:

- low computational cost, well adapted to operational constraints;
- the azimuthal deviations can be estimated from the set of three-dimensional ray paths which compose each table;
- a time and range-dependent atmosphere are handled without significant increase of computation time;
- propagation tables can be built automatically per phase and per bounce order and associated to distinct ray trajectories, unlike fast full waveform modeling techniques such as normal modes or parabolic equation methods (Waxler and Assink 2019).

However, the ray tracing method models the propagation of acoustic waves in the geometrical acoustic limit and exhibits limitations which restrict its utilization in operation, as follows:

- The high-frequency hypothesis is based on the assumption that space and time scales of atmospheric properties (temperature, wind, and density) are much larger than acoustic wave scales. All phases cannot be modeled by ray tracing as the high-frequency approximation made in the Eikonal equation does not account for diffraction (Gainville et al. 2009) which can explain the leakage of acoustic energy out of geometric acoustic ducts. The normal mode technique efficiently overcomes this limitation (Assink et al. 2019) thanks to its capability to calculate separately frequency-dependent modes for phase velocities which are sensitive to borderline cases (i.e., for which $C_{\text{eff-ratio}}$ is close to 1).
- Ray tracing is not sensitive to fine-scale atmospheric structures such as turbulence and gravity waves, as diffraction is the mechanism responsible for partial wave refractions on such small structures (e.g., Kulichkov 2009; Kulichkov et al. 2010; Kulichkov et al. 2019).
- To improve the location result, normal mode techniques can incorporate a probabilistic description of propagation models by applying a perturbative approach (e.g., Millet et al. 2007; Cugnet et al. 2019).

The long-range propagation is simulated here using the Windy Atmospheric Sonic Propagation ray theory-based method (WASP-3D) which accounts for the spatiotemporal variations of the horizontal wind terms along the raypaths in spherical coordinates (Virieux et al. 2004). This method provides all the required kinematic parameters of each ray (travel time, incidence angle, and azimuth deviation) for comparisons with measurements. It is worth highlighting that so far, despite its identified limitations, ray tracing is the only propagation code which allows azimuthal deviations at telesonic ranges to be estimated with reasonable computation times and propagation tables to be built automatically.

For each source to station propagation path, 11 equally spaced azimuths within an interval of $\pm 10°$ centered on the true bearing are considered. In each direction, 200 rays are launched, with elevation angles ranging between 0 and 40° from the horizontal and a step of 0.2°. Among the 2200 (200×11) simulated trajectories, only rays intersecting a volume of 20 km radius, 2 km thickness, centered on the station are selected. These rays are automatically classified and labeled depending on their turning heights and number of ground reflections before reaching the station. Rays refracting below 15 km are labeled as Iw (tropospheric), between 15 and 70 km as Is (stratospheric), and above 70 km as It (thermospheric). A suffix indicating the bounce order is appended to the label. By applying this procedure, which is preferred to costly eigenray techniques, statistics on set of rays which compose each table are calculated. Extracted celerity models and azimuthal deviations are median values of rays of each table.

The celerity model is associated to each arrival which has been labeled following the methodology presented in Sect. 9.2. At I51 GB, in addition to the celerity models, azimuthal corrections are also considered.

Because no closer station exists between the source and I51 GB (the path is purely oceanic), branches cannot be identified and the five recorded arrivals cannot be labeled without simulations. In Fig. 9.10, a comparison of ray simulations with

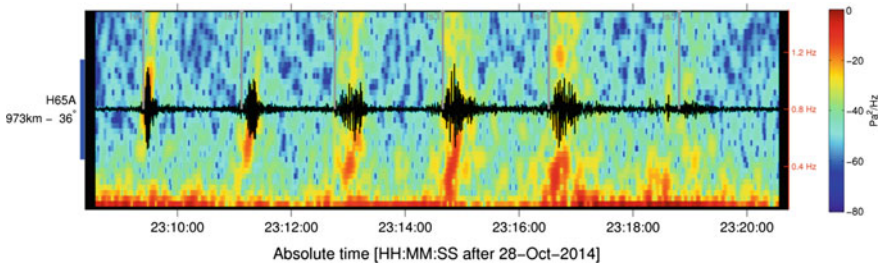

Fig. 9.11 Evidence of a dispersive tropospheric signature on the stratospheric arrivals at station H65A, located 973 km North-East of the Antares event. A fraction of the energy ducted in the narrow tropospheric duct leaks upwards by diffraction and is refracted back to the ground in the stratopause region. The dispersive pattern is conserved during the stratospheric propagation and is less pronounced for higher incidence angles: Is4 and Is5 exhibit less dispersion than Is1 and Is2

the signals suggest that the first recorded phase is Is3 and the last one is Is7. I51 GB is the only array of the IMS network that detected the event. This station consists of four elements with an aperture of 2.4 km. PMCC detections have been calculated with the DTK-PMCC software by applying a 1/3rd log-scaled frequency band configuration (Garcés 2013). The detection results are displayed by rectangles in the time-frequency space on Fig. 9.10, superimposed upon the waveforms. Element I51H1, which was significantly noisier than the 3 other elements, was not used for the calculation. Colored rectangles represent trace velocity values increasing with time (from 350 m/s for Is3–370 m/s for Is7) as the elevation angle of the waves increases with the bounce order. Such an observation is typical for ground to ground propagation (e.g., Ceranna et al. 2009). Ray simulations coupled with array processing confirm that stratospheric phases are associated with slow celerity branches for waves propagating at shallow elevation angles. Fast arrivals exhibit significantly higher trace velocities. At I51 GB, 10 measures are used for the source location: five arrival times and five back azimuths together with celerity models and azimuthal deviations derived from ray tracing simulations.

9.3.2 Extension of Propagation Branches

For TA stations, stratospheric ray branches North-East of the event are not as clear as the ones at I51 GB. In Fig. 9.12, ray simulations are compared to the waveforms at 14 stations, with azimuths ranging from 26° to 36°. Unlike at station I51 GB, the first two stratospheric bounces (in blue) are range limited and do not extend beyond 1000 km, as observed on the waveforms. Thus, remote observations cannot be used for location as no Is1 rays reach stations above 350 km. This is explained by the strong tropospheric duct which traps all rays with the lowest incidence angles. By considering refraction effects only, waves propagating at shallow angles cannot escape into the stratosphere. However, a fraction of this energy leaks in the

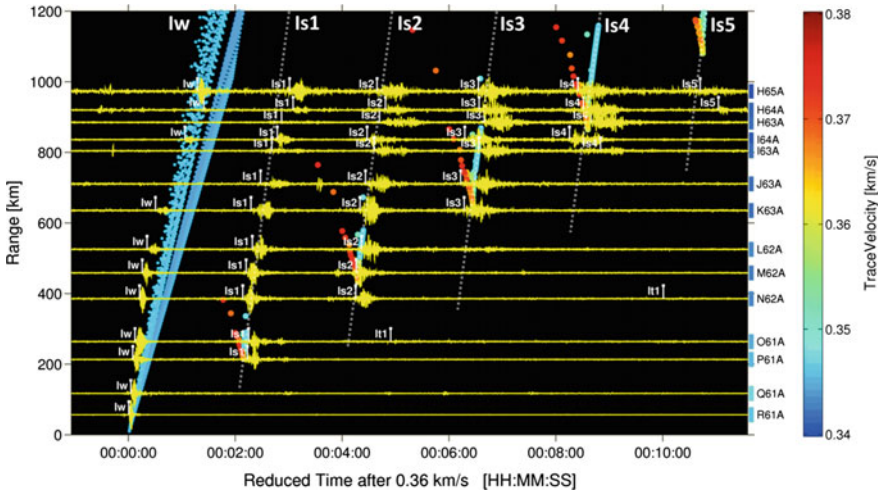

Fig. 9.12 Ray tracing results for 14 stations located North-East of the event, in the 26–36° azimuth range. Ray bounces superimposed in the range/time space allow identifying tropospheric (Iw) and stratospheric (Is) arrivals, from Is1 to Is5. The colorbar codes the ray trace velocity (and associated wave incidence angle). Due to the strong interaction between the tropospheric and the stratospheric ducts, ray tracing cannot explain all recorded arrivals. The manual extension of the stratospheric branches represented by dashed gray lines allows here capturing diffraction effects

stratospheric duct and can be observed at stratospheric distances. Evidence of that phenomenon is the dispersive pattern of some stratospheric arrivals observed in Fig. 9.11.

Due to the high-frequency approximation intrinsic to ray tracing techniques, this diffractive effect cannot be modeled. Rays with higher incidence angles escape from the tropospheric duct which explains the increase in ray bounce density with increasing bounce order: Is3 and Is4 tables can correctly be built with the methodology described above, without being perturbed by the tropospheric duct.

In order to work around those limitations, stratospheric branches are extended manually to build all stratospheric tables for stations that have an effective sound speed ratio larger than 1. This extension is represented by gray lines on Fig. 9.12. In a range-independent atmosphere, slow celerity branches are parallel when moving away from the caustic (shown by gray dashed lines on Fig. 9.10). For the sake of simplicity, the extension is done in parallel to the well-defined Is4 branch (see Fig. 9.12). Such branch extensions are also justified by classical interaction between the acoustic wave field and small-scale atmospheric structures such as gravity waves, which tend to lengthen the location extent of each bounce area. Finally, celerity models for which no rays are intercepted in the vicinity of the stations are built manually and associated with the corresponding measures. All measures and associated models are summarized in the Appendix (Table 9.1).

This method is valid for stratospheric arrivals only if a geometric duct is predicted. For the “Isdiff” branch, as identified on Fig. 9.9b, the effective sound speed

at the stratopause is lower than the sound speed at the ground level. In such conditions, no stratospheric extension is possible because all rays escape into the thermosphere. As a consequence, such arrivals cannot be used for location (represented as orange lines in Table 9.1).

The methodology for building propagation tables is also valid for thermospheric arrivals. The interaction with the tropospheric duct is not an issue like for stratospheric arrivals because thermospheric arrivals are recorded South-West of the event, in directions where the tropospheric duct does not exist. In Fig. 9.13, ray bounces are overlaid to the waveforms at 11 stations located South-West of the event, with azimuths ranging from 222 to 232°. Above 90 km altitude, the effective sound speed is derived from the MSIS-00 empirical model (Picone et al. 2002) for the temperature and HWM-07 (Drob et al. 2008) for the wind speed. Between 80 and 90 km, these empirical models are connected to ECMWF wind and temperature profiles by applying a cubic spline curve fitting approach. Even if dynamical processes in the mesosphere and lower thermosphere are not well resolved by Numerical Weather Prediction (NWP) products (e.g., Le Pichon et al. 2005, 2015), the predicted arrival times are generally consistent with the observations (Fig. 9.13) even if all arrivals cannot be explained.

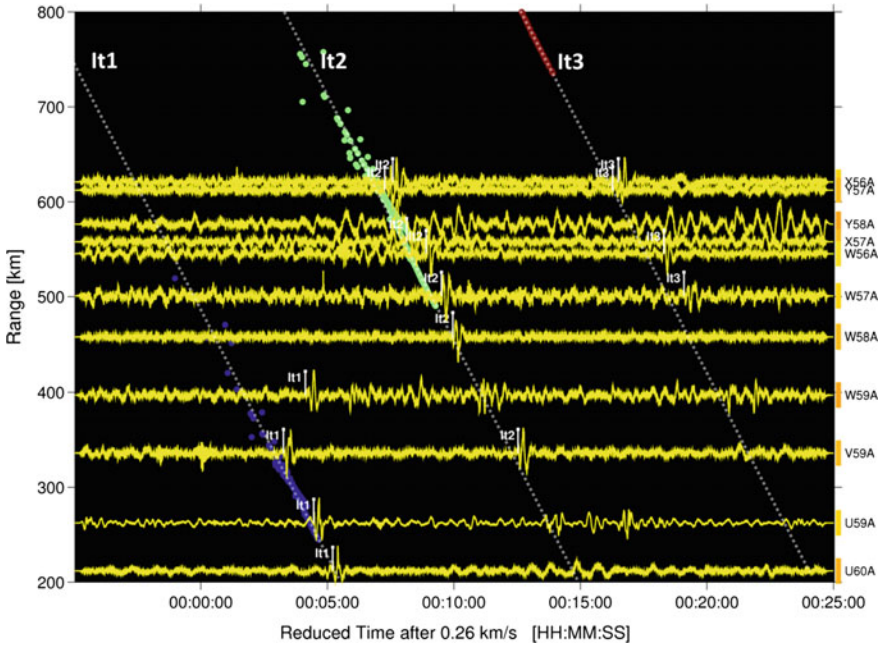

Fig. 9.13 Ray tracing results for 11 stations located southwest of the event, in the 222–232° azimuth range. Ray bounces superimposed in the range/time space allow identifying thermospheric arrivals, from It1 to It3. Colors represent the bounce order. Compared with modeling, thermospheric bounces occur at shorter distances from the source

Of specific interest are bounces occurring at short distances from the source, which is uncommon for thermospheric returns. For example, the first thermospheric bounce in the direction of U60A is observed at 212 km, the second thermospheric bounce at 336 km (V59A) and the third thermospheric bounce at 500 km. Such short distances are not explained by ray tracing and would deserve to be studied. They are probably the results of poorly constrained models, combined with unpredicted diffraction effects.

The branch extension process has to be done again but this time for shorter distances, unlike stratospheric phases for which the extensions had to be done for larger distances. It1, It2, and It3 tables can thus be built even when no thermospheric rays are intercepted. All measures and associated models are summarized in Table 9.1. The only two arrivals not used for the location are It4 (orange lines in Table 9.1).

9.3.3 Source Localization

The localization procedure used in operations at the French National Data Center (NDC) is a grid search algorithm, in which both arrival times and back azimuths are taken into account and weighted. The weights associated with the arrival times and back azimuths are referred as Tweight and Bweight, respectively. Since the origin time is not known, differential travel times are considered for all possible pairs of stations. The localization procedure is described as follows:

- For each two-station combination, the differential travel times are computed for each point of the grid and linearly weighted (if the difference is equal to zero, the corresponding weight is one; if the difference is larger than Tweight, the corresponding weight is null).
- For each back azimuth measure, the differential is computed at each point of the grid and linearly weighted (if the difference is equal to zero, the corresponding weight is one; if the difference is larger than Bweight, the corresponding weight is null).
- All obtained weighted functions are added up in order to provide a two-dimensional probabilistic density function, where its minimum provides the best location.
- The origin time is the median value estimated from the resulting spatial location and celerity models.

Tweight and Bweight are typically taken equal to 300 s and 10°, respectively. The grid size, centered on the Antares event, is 1000 km × 1000 km with a resolution of 500 m. In order to provide a realistic picture of the location, propagation models are randomly perturbed with a uniform distribution centered on the ray tracing results. A maximum perturbation of 10 m/s is taken for the celerity and 3° for the azimuth (Ceranna et al. 2009). The localization procedure is performed 500

times. The 95% confidence ellipse is finally calculated from the location distributions. Two types of locations are computed: one using empirical propagation tables and one using propagation tables derived from ray tracing simulations. The ground truth location is 2014/10/28 22:23:03-37.834 N, 75.488 W.

- *Tables derived from ray tracing*. 176 of the 185 measures are used. Only phases that belong "Isdiff" branch and It4 are not used for the reasons provided above. The obtained location is 2014/10/28 22:23:01-37.83 N, 75.76 W. The location and 95% confidence ellipse are plotted in Fig. 9.14a. The exhaustive list of measured arrival times, measured back azimuths, celerity models, azimuthal deviations, and residuals for both time and back azimuth are summarized in Table 9.1. Peak-to-peak amplitudes are also provided for information. The location is found 2 km East of ground truth information with a difference in origin time of 2 s. The ellipse major axis is 10 km long. Despite significant time residuals, which reach one minute for some thermospheric phases and several tens of seconds for stratospheric phases, the obtained location result is consistent given the large number of measures. Without the TA network, considering only the sparse IMS network, the location could not be obtained.
- *Empirical tables*. Only one type of phase per station is used. When several stratospheric arrivals are measured at a station, only the first one is considered with a celerity model set to 300 m/s. When several thermospheric arrivals are measured on a station, only the first one is considered with a celerity model set to 250 m/s. The celerity model for tropospheric phases is 340 m/s. Finally, 99 of the 185 measures are used in that configuration. The obtained location is 2014/10/28 22:23:47-38.11 N, 74.74 W. The location and 95% confidence ellipse are plotted in Fig. 9.14b. Compared with the location obtained with propagation

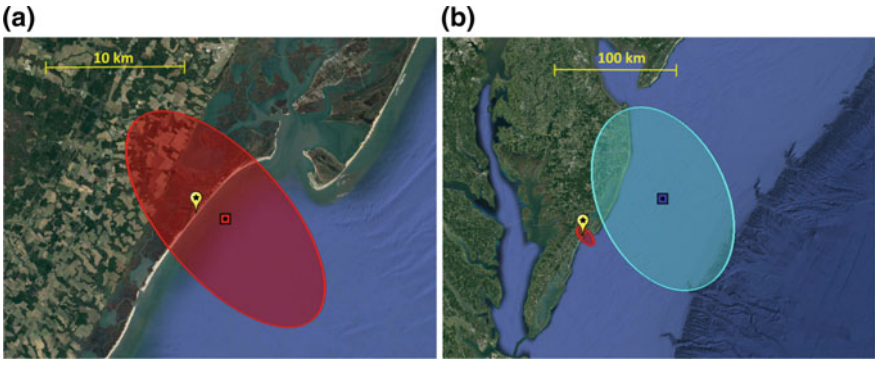

Fig. 9.14 Location results and associated 95% confidence ellipses. **a** In red from propagation tables obtained with ray tracing (176 measures), **b** in blue with phase-dependent empirical Tables (99 measures). While the first configuration provides accurate location (2 km error in space and 2 s error in origin time), the second configuration yields poor result (73 km error in space and 44 s error in time). With the uncommon celerity ranges associated to the different types of phases, the Antares location using empirical tables is not that accurate, with a confidence ellipse which does not include the true location (yellow pin)

tables derived from ray tracing, the location using empirical tables is worse. The spatial location is 73 km North-East of ground truth and the difference in origin time is 44 s. The ellipse major axis length is 80 km. Despite the density of the recording network and the amount of measures used, the final location remains far from the ground truth. One explanation is the uncommon atmospheric features at the time of the Antares event which are the cause of the unexpected celerity ranges when compared to those already reported in the literature (e.g., fast tropospheric and stratospheric phases and thermospheric phases with celerity much lower than typical values). It is worth noting that the large 95% confidence ellipse does not include the ground truth location, suggesting that model errors have been underestimated.

9.4 Attenuation of Stratospheric Phases

Depending on the atmospheric wind structure, infrasonic waves may propagate in acoustic waveguides between the ground and troposphere, stratosphere and lower thermosphere. One dominant factor influencing infrasound detection is the seasonal oscillation of the dominant East-West (zonal) component of the stratospheric wind flow. This oscillation, clearly captured in climatological wind models, controls to first order the ground locations where infrasound signals are expected to be detected since detection capability is enhanced downwind (Drob et al. 2003). Thus, in order to better interpret the recorded signals, it is important to model the detection capability of the monitoring infrasound network by predicting the signal amplitude at any source location of interest, and further evaluate whether the signal is detectable above the noise level at the receivers. A frequency-dependent semiempirical attenuation relationship derived from massive range-independent parabolic equation (PE) simulations has been developed (Le Pichon et al. 2012). This relation accounts for realistic down- and counter-wind scenarios in the stratosphere, and horizontal wind perturbations induced by gravity waves which play an important role in returning acoustic energy to the ground (Gardner et al. 1993). Beyond the first stratospheric bounce, this relation describes the attenuation by accounting for the geometrical spreading and dissipation of both stratospheric and thermospheric waves. In the far-field, the attenuation essentially varies in R^{β}, where R is the propagation range (in km) and β a dimensionless parameter which depends on the frequency and effective sound speed ratio at 50 km.

This frequency-dependent semiempirical attenuation relationship has been used to construct attenuation maps at three different frequencies: 0.3, 1, and 2 Hz (Fig. 9.15). According to the modeling, the stratospheric duct starts refracting acoustic energy back to the ground for $C_{\text{eff-ratio}}$ larger than one, hence decreasing the transmission loss. In case of downwind propagation ($C_{\text{eff-ratio}} > 1$, i.e., the case for the most easterly stations), the attenuation parameter β is roughly constant in the studied frequency range ($\beta = -0.92 \pm 0.05$). This behavior is in contrast to

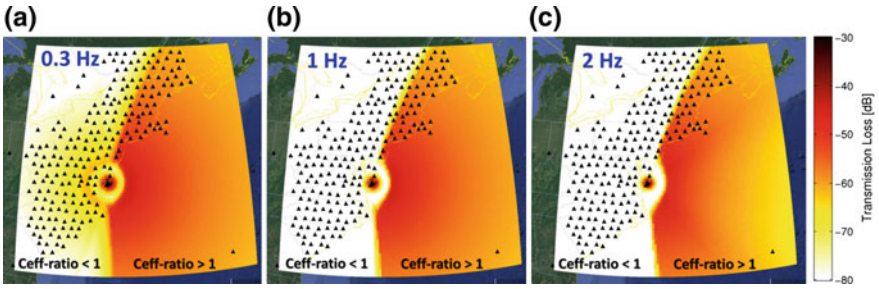

Fig. 9.15 Geographical distribution of the pressure wave attenuation at three frequencies: **a** 0.3 Hz, **b** 1 Hz and **c** 2 Hz. The color scale codes the attenuation (in dB) calculated from the source at a reference distance of 1 km to the receiver. Geographical and frequency-dependent effects are depicted: according to the station location relative to Ceff-ratio = 1 border, a strong frequency dependence of the transmission loss is observed

propagation occurring in upwind direction. In such situation ($C_{\text{eff-ratio}} < 1$; i.e., the case for the most westerly stations), sound propagating upwards is more attenuated due to the low particle density and nonlinear dissipation in the thermosphere (Sutherland and Bass 2004). Between 0.3 and 2 Hz, a much stronger attenuation is predicted for $C_{\text{eff-ratio}} = 0.9$, with $\beta = -1.25 \pm 0.11$ at 0.3 Hz and $\beta = -1.78 \pm 0.12$ at 2 Hz, respectively. The delimitation between these two regions ($C_{\text{eff-ratio}} = 1$) is clearer at higher frequencies (Fig. 9.15c).

In the $C_{\text{eff-Ratio}} < 1$ region, the transmission loss is strongly frequency-dependent. At 0.3 Hz (Fig. 9.15a), the first thermospheric bounce is visible with a predicted attenuation as high as 70 dB at 600 km. At 1 and 2 Hz, the attenuation is larger than 80 dB and the shadow zone is deeper.

In the $C_{\text{eff-Ratio}} > 1$ region, the differences occur at ranges larger than 500 km and at higher frequencies. For example, at I51 GB station, the predicted transmission loss is comparable at 0.3 and 1 Hz while it is 10 dB larger at 2 Hz.

9.4.1 *Attenuation of Stratospheric Phases as a Function of Frequency and $C_{\text{eff-ratio}}$*

To compare the predicted and measured transmission losses (extracted from amplitudes of picked phases summarized in Table 9.1) as a function of range, frequency, and $C_{\text{eff-ratio}}$, two different subsets of stations have been considered.

A first set of eight stations has been selected at a range of about 600 km (±50 km) (Fig. 9.16a). This configuration allows focusing on the attenuation of the stratospheric phases as of function a frequency and $C_{\text{eff-ratio}}$. The background noise level along this 500 km long line is low enough to identify stratospheric arrivals at a constant range from the event, with $C_{\text{eff-ratio}}$ values ranging evenly from 1.15 (red colors indicating downwind situation for eastern stations) down to 0.9 (blue colors

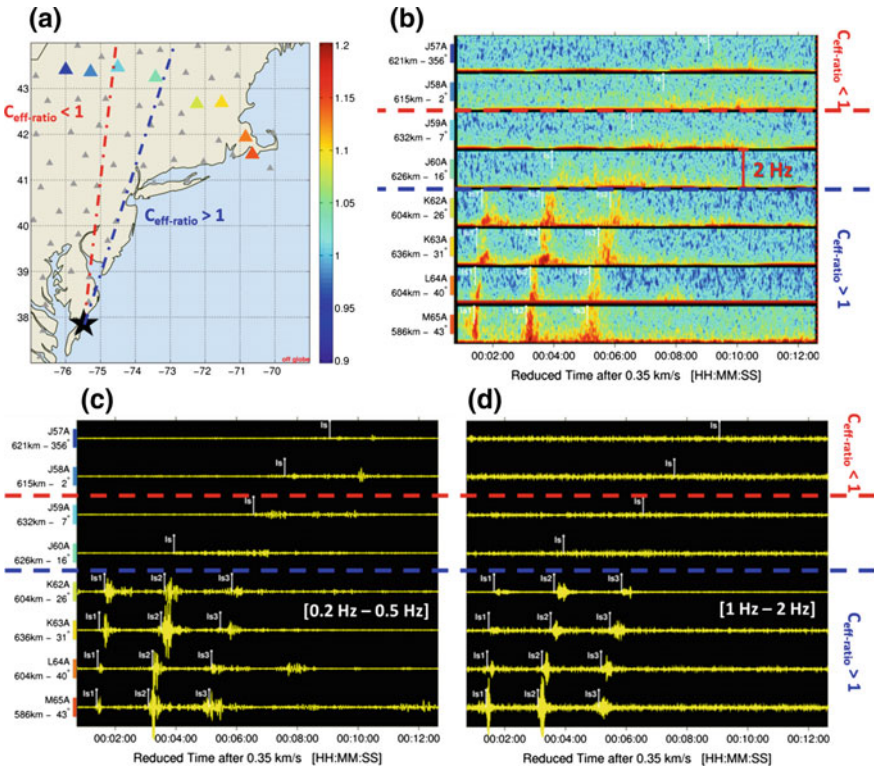

Fig. 9.16 Attenuation of stratospheric phases as a function $C_{eff\text{-}ratio}$ and signal frequency. Eight stations have been thoroughly chosen at a fixed distance from the Antares explosion (about 600 km) with continuous decreasing values of $C_{eff\text{-}ratio}$, from 1.15 down to 0.9. Stations are highlighted in color in panel (**a**) according to $C_{eff\text{-}ratio}$ values. The corresponding spectrograms between 0 and 2 Hz are plotted in panel (**b**), waveforms filtered between 0.2 and 0.5 Hz are plotted in panel (**c**), and waveforms filtered between 1 and 2 Hz are plotted in panel (**d**). Waveforms and spectrograms are sorted by $C_{eff\text{-}ratio}$ from top to bottom. The same amplitude scales are applied to all stations. $C_{eff\text{-}ratio} = 1$ borders are plotted as thick dashed lines on all subpanels, in red without taking into account crossed winds, in blue taking into account crossed winds. In the $C_{eff\text{-}ratio} > 1$ region, east of the blue line, broadband well-separated arrivals are observed. Beyond $C_{eff\text{-}ratio} = 1$ border, west of the red line, high frequencies are strongly attenuated, as shown in the spectrograms and waveforms, and stratospheric arrivals become narrow low-frequency band diffuse signals ("Isdiff" branch discussed in Sect. 2.4.4). The transition occurs when $C_{eff\text{-}ratio} = 1$ blue border is crossed, i.e., when crossed winds are taken into account

indicating upwind situation for western stations). This single line is clearly visible in Fig. 9.1 with the alignment of dark blue stations with low background noise. The corresponding spectrograms (Fig. 9.16b) and waveforms filtered in two different frequency bands (Fig. 9.16c: low-frequency band between 0.2 and 0.5 Hz, Fig. 9.16d: high-frequency band between 1 and 2 Hz) are represented. The same amplitude scales have been applied to the waveforms. The $C_{eff\text{-}ratio} = 1$ border

without taking crossed winds into account is shown by a red dashed line on all subpanels, and a dashed blue line that takes into account crossed winds.

- As predicted, in the geometrical ducting region ($C_{eff\text{-}ratio} > 1$, East of blue dashed line), low and high-frequency signals are efficiently ducted and the broadband feature is conserved whatever the value of $C_{eff\text{-}Ratio}$ above 1. It is noteworthy that when downwind propagation occurs, any significant wind component in the stratosphere, such that $C_{eff\text{-}Ratio} > 1$, comparable signal attenuation is predicted. This feature contradicts the Los Alamos National Laboratory (LANL) relation (Whitaker 2003), which predicts an exponential variation in signal amplitude with changing wind speed. Our model attenuation follows an approximately binary variation with the effective sound speed ratio.
- Crossing westwards the $C_{eff\text{-}Ratio} = 1$ border, high frequencies are strongly attenuated, as shown in Fig. 9.15. This effect is clearly visible on both spectrograms and waveforms: when the $C_{eff\text{-}ratio} < 1$ region is reached (dashed blue line), only low frequencies remain. Broadband well-separated arrivals change into narrow low-frequency band emergent signals. These low-frequency stratospheric arrivals labeled as "Isdiff" branch (Sect. 2.4.4) are not used for the location because they are not modeled by ray tracing (Sect. 9.3). As opposed to the $C_{eff\text{-}Ratio} > 1$ region, low-frequency signal amplitudes depend on $C_{eff\text{-}Ratio}$ values (e.g., J59A has stronger amplitude than J57A while M65A has comparable amplitude to K63A).
- Unlike the prediction, it is clear in Fig. 9.16c that such low-frequency diffuse signals already start being observed at $C_{eff\text{-}ratio}$ values larger than one (i.e., below the red dashed line, Fig. 9.16c). At any location, $C_{eff\text{-}ratio}$ is derived from the averaged stratospheric winds projected in the direction of propagation, without taking into account the crossed wind component. In strong stratospheric jet conditions (reaching 80 m/s at the turning heights, see Fig. 9.2d, e), the strong advection shifts the $C_{eff\text{-}ratio} = 1$ border eastwards. With azimuthal deviations simulated by ray tracing (Sect. 9.3), the border is shifted by 9.2° (dashed blue line on Fig. 9.16). By applying this correction, the frequency contents of the detected signals are consistent with the predicted frequency-dependent attenuations. Such a three-dimensional effect should be taken into account when $C_{eff\text{-}ratio}$ is close to 1 and strong crossed winds occur. Full waveform modeling techniques in which propagations is simulated in a vertical plane, such as normal modes or parabolic equation method, would fail in predicting waveform shapes and amplitudes in such directions if crossed winds are not considered. In addition, when $C_{eff\text{-}ratio}$ is close to 1, the predicted arrival time, amplitude and duration of the signals become more sensitive to wind perturbations induced by unresolved small-scale structures (e.g., Kulichkov et al. 2010; Green et al. 2011).

9.4.2 *Attenuation of Stratospheric Phases as a Function of Range and Frequency*

A second set of eight stations has been selected with constant $C_{eff\text{-}ratio}$ value of 1.05 with distances ranging from 386 to 918 km, as shown in Fig. 9.17a. This configuration allows focusing on the attenuation of the stratospheric phases as a function

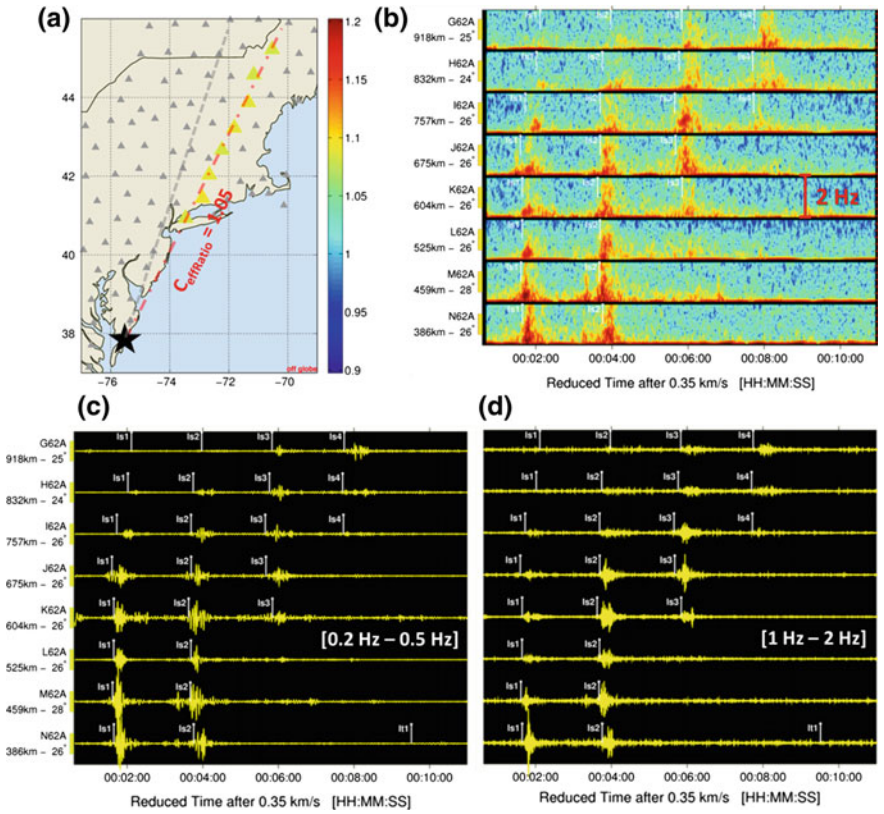

Fig. 9.17 Attenuation of stratospheric phases as a function of range and signal frequency, inside geometrical ducting regions. Eight stations have been thoroughly chosen with a fixed $C_{eff\text{-}ratio}$ value of 1.05 with continuous increasing ranges, from 386 to 918 km. Stations are highlighted in color in panel (**a**) according to their $C_{eff\text{-}ratio}$ values. Corresponding spectrograms between 0 and 2 Hz are plotted in panel (**b**), waveforms filtered between 0.2 and 0.5 Hz are plotted in panel (**c**), and waveforms filtered between 1 and 2 Hz are plotted in panel (**d**). Waveforms and spectrograms are sorted by distance from bottom to top, and the same amplitude dynamics is applied to all stations. Cross winds-corrected $C_{eff\text{-}ratio} = 1$ border is plotted as a gray dashed line on the map and $C_{eff\text{-}ratio} = 1.05$ is plotted as a red dashed line. As predicted, the attenuation of most energetic arrivals varies in $R^{-0.92}$ and is frequency independent, at first order. Broadband frequency signals are efficiently ducted especially at times when ray tracing predicts a large density of rays reaching the stations (Fig. 9.12). Diffracted arrivals associated to the branch extensions presented in Sect. 3.2 have lower frequency contents, as shown in the spectrograms and waveforms

of range and frequency inside geometrical ducting regions. In particular, the attenuation can be studied along a line of about 500 km with a regular inter-station spacing, where values of $C_{\text{eff-Ratio}}$ are comparable. The corresponding spectrograms (Fig. 9.17b) and waveforms filtered in two different frequency bands (Fig. 9.17c: between 0.2 and 0.5 Hz; Fig. 9.17d: between 1 and 2 Hz) are represented. The same amplitude dynamics is applied to the waveforms. The cross wind-corrected $C_{\text{eff-ratio}} = 1$ border is plotted as a gray dashed line on the map and the $C_{\text{eff--ratio}} = 1.05$ line is plotted in red.

- As predicted, at large distances, the attenuation of the most energetic arrivals varies in R_β, where $\beta = -0.92$ is almost frequency independent (higher frequencies are slightly more attenuated). While the energy varies in R_β, the amplitude of most energetic arrivals remains a good proxy for such a qualitative study.
- Broadband frequency signals are efficiently ducted in geometrical ducting regions, especially at times when ray tracing predicts a large density of rays reaching the stations (see Fig. 9.12). Diffracted arrivals associated to the branch extensions presented in Sect. 3.2 have lower frequency contents, as shown on the spectrograms and waveforms. On the farthest stations G62A and H62A, Is1 and Is2 arrivals have much narrower and lower frequency contents than Is3 and Is4 which are broadband.

9.5 Discussions and Concluding Remarks

The results presented in this study provide a good overview of the operational capabilities of dense regional infrasound networks to study events of interest for the Comprehensive Nuclear-Test-Ban verification regime. They also highlight the limitations of routinely used codes, especially concerning effects of unresolved gravity waves which play a significant role in infrasound propagation.

The amount and variety of infrasound arrivals associated with the Antares explosion make this event unique. Due to a large high-pressure system centered offshore in the western Atlantic and steady night conditions, most of the stations exhibited low acoustic background noise levels. In addition to these favorable observation conditions, several wind jets at altitudes ranging from ground to the lower mesosphere were all blowing North-Eastwards. Consequently, stations located North-East of the explosion along the coastline recorded tens of stratospheric and tropospheric infrasound arrivals up to 1100 km. In the opposite direction, in the South-West quadrant, stations recorded several tens of

thermospheric arrivals at ranges up to 1000 km. 175 phases were identified as tropospheric, stratospheric or thermospheric arrivals on 73 stations of the TA. The SNR is often larger than 1 and the phase identification is not ambiguous due to the density of the recording stations, even if standard array processing methods cannot be applied. The IMS station I51 GB located in Bermuda, 1154 km South-Eastwards, also recorded five stratospheric phases predicted by ray tracing simulations. Overall, 74 stations detected the event and 180 phases were manually identified, picked, and labeled. The celerity range of the recorded phases is exceptionally broad, from 360 m/s for some tropospheric phases, down to 160 m/s for some thermospheric phases. Using phase-dependent propagation tables derived from ray tracing simulations, the source was accurately located 2 km East of ground truth information with a difference in origin time of 2 s.

For comparison, the most energetic event ever recorded so far by the IMS network is the Chelyabinsk meteor of the February 15, 2013, from which the acoustic energy was estimated to be equivalent to around 500 kt of TNT (Le Pichon et al 2013). 18 TA infrasound sensors recorded this event up to 15,000 km and 56 infrasound phases were associated with the analysts at the IDC (Mialle et al. 2019). More generally, most of the acoustic events built by the IDC from the sparse global IMS infrasound network (the mean inter-station distance is about 2000 km) associate only a few infrasound stations and arrivals. In favorable observation conditions, a limited number of measures allow in-depth studies considering both source localization and characterization (Ceranna et al. 2009; Green et al. 2009). However, for events of smaller energy, the use of dense regional seismo-acoustic networks clearly improves the detection and location capability of the infrasound IMS network (e.g., Gibbons et al. 2015; Che et al. 2017).

Further studies shall be pursued to model a more realistic picture of infrasound propagation for the Antares event. The high-quality data and the unprecedented amount and variety of observed infrasound phases on a dense network would provide a statistical approach for evaluating atmospheric models, numerical propagation modeling and localization methods. Studies of specific interest for the nuclear explosion monitoring regime are to:

- Assess localization procedures and quantify associated uncertainties in space and time considering an unusual amount of measures.
- Study the dispersion and ground/ocean interaction of tropospheric phases propagating within a thin and unstable advected waveguide at ranges up to 1000 km (27 tropospheric phases were recorded with celerities ranging from 340 to 360 m/s).
- Study the attenuation of stratospheric phases. Different numerical propagation modeling methods could be tested and compared (e.g., Le Pichon et al. 2012; Waxler and Assink 2019).

- Study thermospheric propagation up to 1000 km (It1 to It4 branches have clearly been identified). 46 thermospheric arrivals were recorded from this single event, which is unprecedented. Corresponding celerities extend from very low values (160 m/s for It3 at 500 km) to typical values (250 m/s). A unique collection of shapes such as "U", "N", and shock waves, generated by nonlinear propagation in the thermosphere and caustics, are of great interest to improve our knowledge of the thermosphere (e.g., Assink et al. 2012). Numerical explorations with fully time- and range-dependent wave propagation techniques accounting for nonlinear propagation effects would provide more realistic results while still maintaining computational efficiency (Waxler and Assink, this volume).
- Assess the impact of unresolved small-scale structures in middle atmospheric models induced by naturally occurring gravity waves (e.g., Le Pichon et al. 2015) on the propagation of stratospheric waves could be addressed by considering deterministic (e.g., Green et al. 2011) or stochastic approaches (e.g., Drob et al. 2013). Moreover, due to strong stratospheric cross winds for North/North-East propagation, errors due to three-dimensional effects can be assessed.

Continuing such studies would help to further enhance network performance simulations and optimize future network design in order to monitor infrasonic sources of interest. This is an important step toward a successful monitoring regime for atmospheric or surface events and to act as an effective verification tool in the near future.

Appendix

See Table 9.1.

Table 9.1 Exhaustive list of measured phases and information relative to the location obtained from ray tracing propagation tables. From left to right: station name, phase name, range, arrival time, back azimuth (only for I51 GB), peak-to-peak amplitude in relevant frequency band, celerity model, and azimuthal deviation obtained from ray tracing (only for I51 GB), time residual, back azimuth residual, and final celerity obtained after location. The color of each line represents arrival type: red is tropospheric, green is stratospheric, blue is thermospheric, and orange indicates that the phase has not been used for location because it was not modeled

Station	Phase	Range [km]	Arrival Time [DD/MM/YYYY HH :MM :SS]	Measured θ [°]	Peak-to-Peak Amplitude [Pa]	Celerity Model [km/s]	Δθ [°]	Time Residual [s]	θ Residual [°]	Celerity [km/s]
S61A	Iw	25	28/10/2014 22:24:11	-	15.2	0.351	-	0.0	-	0.351
R61A	Iw	57	28/10/2014 22:25:41	-	48	0.350	-	1.6	-	0.353
Q61A	Iw	117	28/10/2014 22:28:31	-	3.3	0.350	-	4.3	-	0.355
Q60A	Iw	134	28/10/2014 22:29:20	-	0.39	0.350	-	4.1	-	0.353
U61A	It1	188	28/10/2014 22:40:27	-	1.00	0.178	-	7.7	-	0.180
T59A	It1	208	28/10/2014 22:41:51	-	0.76	0.179	-	29.9	-	0.184
P61A	Is1	213	28/10/2014 22:35:09	-	2.0	0.292	-	0.2	-	0.292
U60A	It1	213	28/10/2014 22:41:50	-	0.82	0.186	-	13.8	-	0.189
P61A	Iw	213	28/10/2014 22:33:00	-	1.6	0.352	-	4.8	-	0.355
S58A	It1	229	28/10/2014 22:42:54	-	1.7	0.192	-	2.1	-	0.192
V61A	It1	247	28/10/2014 22:42:53	-	0.78	0.205	-	15.4	-	0.207
O61A	Is1	263	28/10/2014 22:37:31	-	1.3	0.302	-	1.9	-	0.303
O61A	It1	263	28/10/2014 22:40:10	-	0.34	0.253	-	10.5	-	0.256
O61A	Iw	263	28/10/2014 22:35:23	-	1.9	0.349	-	11.3	-	0.355
U59A	It1	264	28/10/2014 22:44:20	-	0.56	0.206	-	0.3	-	0.206
R57A	It1a	273	28/10/2014 22:44:55	-	1.1	0.211	-	-19.7	-	0.208
R57A	It1b	273	28/10/2014 22:46:51	-	0.72	0.191	-	-2.5	-	0.191
O60A	Is1	276	28/10/2014 22:38:19	-	0.14	0.298	-	8.1	-	0.301
O60A	It1	276	28/10/2014 22:41:14	-	0.70	0.251	-	7.6	-	0.252
V60A	It1	280	28/10/2014 22:44:36	-	0.59	0.218	-	-14.2	-	0.216
P57A	It1a	288	28/10/2014 22:44:28	-	2.9	0.221	-	16.3	-	0.224
P57A	It1b	288	28/10/2014 22:44:47	-	1.6	0.219	-	10.4	-	0.220
O57A	It1a	324	28/10/2014 22:44:43	-	0.36	0.251	-	-12.4	-	0.249
O57A	It1b	324	28/10/2014 22:46:04	-	0.30	0.229	-	30.7	-	0.234
W61A	It1	325	28/10/2014 22:46:34	-	0.62	0.225	-	25.9	-	0.230
V59A	It1	337	28/10/2014 22:47:51	-	0.21	0.228	-	-9.7	-	0.226
V59A	It2	337	28/10/2014 22:57:07	-	0.24	0.169	-	-49.5	-	0.165
N61A	Is1	339	28/10/2014 22:41:12	-	1.7	0.309	-	8.0	-	0.311
N61A	It1	339	28/10/2014 22:44:45	-	0.13	0.264	-	-17.1	-	0.260
N61A	Iw	339	28/10/2014 22:39:03	-	0.82	0.348	-	13.6	-	0.353
Q56A	It1	352	28/10/2014 22:48:48	-	0.77	0.229	-	-14.3	-	0.227
W60A	It2	368	28/10/2014 22:57:54	-	0.36	0.177	-	-19.1	-	0.176
N62A	Is1	385	28/10/2014 22:43:02	-	1.8	0.321	-	-3.2	-	0.320
N62A	Is2	385	28/10/2014 22:45:09	-	1.2	0.295	-	-23.6	-	0.290
N62A	It1	385	28/10/2014 22:50:54	-	1.3	0.233	-	-25.5	-	0.230
N62A	Iw	385	28/10/2014 22:41:06	-	1.7	0.349	-	15.5	-	0.354
W59A	It1	398	28/10/2014 22:52:38	-	0.38	0.226	-	-16.4	-	0.224
M61A	Is1	413	28/10/2014 22:44:31	-	0.35	0.323	-	-13.1	-	0.320
M61A	Is2	413	28/10/2014 22:46:36	-	0.61	0.292	-	-2.4	-	0.292
M61A	Iw	413	28/10/2014 22:42:29	-	0.32	0.348	-	18.2	-	0.353
N63A	Is1	432	28/10/2014 22:45:11	-	2.9	0.327	-	-8.5	-	0.325
N63A	Is2	432	28/10/2014 22:47:05	-	1.0	0.304	-	-23.9	-	0.299
N63A	Iw	432	28/10/2014 22:43:20	-	5.7	0.351	-	10.5	-	0.354
V57A	It2	441	28/10/2014 23:01:46	-	0.31	0.193	-	-44.6	-	0.189
M62A	Is1	457	28/10/2014 22:46:28	-	1.4	0.323	-	9.6	-	0.325
M62A	Is2	457	28/10/2014 22:48:32	-	1.4	0.298	-	2.1	-	0.299
M62A	Iw	457	28/10/2014 22:44:32	-	0.99	0.351	-	11.5	-	0.354
W58A	It2	460	28/10/2014 23:02:23	-	0.36	0.189	-	67.2	-	0.195
M63A	Is1	493	28/10/2014 22:48:02	-	1.9	0.333	-	-20.8	-	0.329
M63A	Is2	493	28/10/2014 22:49:57	-	0.87	0.303	-	10.6	-	0.305
M63A	Iw	493	28/10/2014 22:46:12	-	2.7	0.351	-	15.0	-	0.354
W57A	It2	503	28/10/2014 23:04:40	-	0.061	0.202	-	-8.0	-	0.201
W57A	It3	503	28/10/2014 23:14:15	-	0.043	0.164	-	-13.0	-	0.164
L62A	Is1	524	28/10/2014 22:49:41	-	0.61	0.327	-	2.0	-	0.328
L62A	Is2	524	28/10/2014 22:51:44	-	0.66	0.309	-	-23.9	-	0.304
L62A	Iw	524	28/10/2014 22:47:43	-	0.20	0.352	-	6.5	-	0.354
Y59A	It2	525	28/10/2014 23:04:56	-	0.18	0.207	-	26.4	-	0.209
Y59A	It3	525	28/10/2014 23:14:34	-	0.16	0.171	-	-14.3	-	0.170
Q53A	It2	542	28/10/2014 23:06:34	-	0.14	0.204	-	44.3	-	0.207
Q53A	It3	542	28/10/2014 23:15:56	-	0.14	0.171	-	-8.7	-	0.171

(continued)

Table 9.1 (continued)

W56A	It2	547	28/10/2014 23:06:54	-	0.27	0.210	-	-23.2	-	0.208
W56A	It3	547	28/10/2014 23:16:18	-	0.20	0.169	-	37.5	-	0.171
K60A	Is	548	28/10/2014 22:53:09	-	0.18	-	-	-	-	0.303
M64A	Is1	551	28/10/2014 22:50:46	-	1.7	0.335	-	-20.2	-	0.331
M64A	Is2	551	28/10/2014 22:52:29	-	1.5	0.317	-	-30.7	-	0.312
M64A	Is3	551	28/10/2014 22:54:44	-	1.4	0.286	-	24.9	-	0.289
M64A	Iw	551	28/10/2014 22:48:54	-	3.2	0.351	-	15.2	-	0.355
L63A	Is1	556	28/10/2014 22:51:04	-	1.2	0.335	-	-26.0	-	0.330
L63A	Is2	556	28/10/2014 22:52:56	-	0.69	0.308	-	7.1	-	0.310
L63A	Is3	556	28/10/2014 22:55:08	-	0.27	0.287	-	5.8	-	0.288
L63A	Iw	556	28/10/2014 22:49:13	-	1.7	0.348	-	24.6	-	0.353
V55A	It2	558	28/10/2014 23:07:32	-	0.18	0.207	-	25.3	-	0.209
V55A	It3	558	28/10/2014 23:16:48	-	0.15	0.177	-	-77.4	-	0.173
X57A	It2	559	28/10/2014 23:06:56	-	0.34	0.208	-	48.0	-	0.212
L61B	Is1	565	28/10/2014 22:51:34	-	0.25	0.329	-	5.0	-	0.330
L61B	Is2	565	28/10/2014 22:53:41	-	0.28	0.303	-	22.8	-	0.307
L61B	Is3	565	28/10/2014 22:55:59	-	0.22	0.287	-	-9.6	-	0.285
L61B	Iw	565	28/10/2014 22:49:43	-	0.052	0.347	-	24.3	-	0.352
U54A	It2	583	28/10/2014 23:08:56	-	0.15	0.210	-	21.8	-	0.211
U54A	It3	583	28/10/2014 23:18:03	-	0.14	0.178	-	-33.7	-	0.176
M65A	Is1	585	28/10/2014 22:52:18	-	1.4	0.335	-	-14.8	-	0.333
M65A	Is2	585	28/10/2014 22:54:01	-	1.3	0.319	-	-27.6	-	0.314
M65A	Is3	585	28/10/2014 22:56:01	-	0.64	0.292	-	23.3	-	0.295
M65A	Iw	585	28/10/2014 22:50:28	-	4.5	0.351	-	18.2	-	0.355
M66A	Is1	595	28/10/2014 22:52:39	-	1.1	0.334	-	1.9	-	0.335
M66A	Is2	595	28/10/2014 22:54:22	-	1.9	0.318	-	-7.4	-	0.316
M66A	Is3	595	28/10/2014 22:56:19	-	2.3	0.296	-	12.1	-	0.298
M66A	Iw	595	28/10/2014 22:50:56	-	1.6	0.348	-	32.5	-	0.355
K62A	Is1	603	28/10/2014 22:53:26	-	0.44	0.328	-	12.9	-	0.330
L64A	Is1	603	28/10/2014 22:53:13	-	0.46	0.329	-	22.1	-	0.333
K62A	Is2	603	28/10/2014 22:55:24	-	0.40	0.315	-	-27.7	-	0.310
L64A	Is2	603	28/10/2014 22:55:01	-	0.50	0.311	-	20.1	-	0.314
K62A	Is3	603	28/10/2014 22:57:37	-	0.21	0.293	-	-16.2	-	0.290
L64A	Is3	603	28/10/2014 22:56:58	-	0.30	0.302	-	-38.0	-	0.296
L64A	Iw	603	28/10/2014 22:51:25	-	0.70	0.350	-	17.8	-	0.354
Y57A	It2	613	28/10/2014 23:09:33	-	0.36	0.215	-	66.7	-	0.220
Y57A	It3	613	28/10/2014 23:18:34	-	0.12	0.189	-	-82.7	-	0.184
J58A	Is	614	28/10/2014 22:59:53	-	0.11	-	-	-	-	0.278
J57A	Is	621	28/10/2014 23:01:41	-	0.089	-	-	-	-	0.268
V54A	It3	621	28/10/2014 23:19:36	-	0.15	0.184	-	-22.1	-	0.183
X56A	It2	623	28/10/2014 23:10:26	-	0.14	0.221	-	-33.1	-	0.219
X56A	It3	623	28/10/2014 23:19:20	-	0.15	0.180	-	79.6	-	0.184
J60A	Is	625	28/10/2014 22:58:12	-	0.14	-	-	-	-	0.296
J59A	Is	631	28/10/2014 23:00:09	-	0.062	-	-	-	-	0.283
K63A	Is1	635	28/10/2014 22:54:46	-	0.38	0.333	-	-2.4	-	0.333
K63A	Is2	635	28/10/2014 22:56:48	-	0.71	0.310	-	18.2	-	0.313
K63A	Is3	635	28/10/2014 22:58:45	-	0.52	0.296	-	-0.1	-	0.296
K63A	Iw	635	28/10/2014 22:52:59	-	0.15	0.353	-	1.9	-	0.353
L65A	Iw	656	28/10/2014 22:53:50	-	2.5	0.350	-	27.8	-	0.355
J62A	Is1	674	28/10/2014 22:56:46	-	0.33	0.332	-	7.1	-	0.333
J62A	Is2	674	28/10/2014 22:58:52	-	0.45	0.312	-	7.8	-	0.313
J62A	Is3	674	28/10/2014 23:00:51	-	0.71	0.297	-	0.5	-	0.297
J62A	Iw	674	28/10/2014 22:54:55	-	0.096	0.349	-	19.3	-	0.352
I59A	Is	676	28/10/2014 23:01:47	-	0.078	-	-	-	-	0.290
I60A	Is	692	28/10/2014 23:02:36	-	0.089	-	-	-	-	0.291
J63A	Is1	710	28/10/2014 22:58:25	-	0.26	0.337	-	-20.1	-	0.334
J63A	Is2	710	28/10/2014 23:00:23	-	0.36	0.317	-	-2.0	-	0.316
J63A	Is3	710	28/10/2014 23:02:10	-	0.68	0.305	-	-23.3	-	0.302
X54A	It3	720	28/10/2014 23:23:55	-	0.18	0.195	-	36.4	-	0.197
X54A	It4	720	28/10/2014 23:33:29	-	0.14	-	-	-	-	0.170
I62A	Is1	756	28/10/2014 23:00:47	-	0.26	0.336	-	-18.2	-	0.333
I62A	Is2	756	28/10/2014 23:02:45	-	0.19	0.317	-	-1.6	-	0.317
I62A	Is3	756	28/10/2014 23:04:43	-	0.99	0.306	-	-29.6	-	0.302
I62A	Is4	756	28/10/2014 23:06:47	-	0.14	0.284	-	29.7	-	0.288
I63A	Is1	803	28/10/2014 23:02:58	-	0.070	0.333	-	17.5	-	0.335

(continued)

Table 9.1 (continued)

I63A	Is2	803	28/10/2014 23:04:53	-	0.14	0.324	-	-35.4	-	0.320
I63A	Is3	803	28/10/2014 23:06:50	-	0.42	0.302	-	34.2	-	0.305
I63A	Is4	803	28/10/2014 23:09:07	-	0.15	0.289	-	15.4	-	0.290
H62A	Is1	831	28/10/2014 23:04:40	-	0.070	0.336	-	-29.0	-	0.332
H62A	Is2	831	28/10/2014 23:06:24	-	0.098	0.317	-	16.3	-	0.319
H62A	Is3	831	28/10/2014 23:08:25	-	0.25	0.302	-	30.4	-	0.305
H62A	Is4	831	28/10/2014 23:10:21	-	0.21	0.296	-	-33.0	-	0.293
I64A	Is1	835	28/10/2014 23:04:33	-	0.52	0.338	-	-17.9	-	0.335
I64A	Is2	835	28/10/2014 23:06:13	-	0.37	0.323	-	-4.6	-	0.322
I64A	Is3	835	28/10/2014 23:08:03	-	0.98	0.309	-	4.3	-	0.309
I64A	Is4	835	28/10/2014 23:10:01	-	0.67	0.298	-	-18.6	-	0.296
I64A	Iw	835	28/10/2014 23:02:49	-	0.20	0.353	-	-20.5	-	0.350
H63A	Is1	884	28/10/2014 23:06:53	-	0.034	0.334	-	10.9	-	0.336
H63A	Is2	884	28/10/2014 23:08:43	-	0.12	0.325	-	-19.1	-	0.322
H63A	Is3	884	28/10/2014 23:10:41	-	0.31	0.306	-	25.9	-	0.309
H63A	Is4	884	28/10/2014 23:12:40	-	0.26	0.302	-	-49.1	-	0.297
G62A	Is1	917	28/10/2014 23:08:53	-	0.042	0.335	-	-10.3	-	0.333
G62A	Is2	917	28/10/2014 23:10:44	-	0.064	0.326	-	-45.9	-	0.320
G62A	Is3	917	28/10/2014 23:12:36	-	0.15	0.311	-	-27.8	-	0.308
G62A	Is4	917	28/10/2014 23:14:30	-	0.53	0.301	-	-41.4	-	0.297
H64A	Is1	919	28/10/2014 23:08:43	-	0.14	0.335	-	3.1	-	0.335
H64A	Is2	919	28/10/2014 23:10:27	-	0.20	0.321	-	18.8	-	0.323
H64A	Is3	919	28/10/2014 23:12:12	-	0.64	0.314	-	-26.1	-	0.311
H64A	Is4	919	28/10/2014 23:14:09	-	0.60	0.303	-	-36.6	-	0.300
H64A	Is5	919	28/10/2014 23:16:41	-	0.14	0.287	-	-16.9	-	0.285
H64A	Iw	919	28/10/2014 23:07:03	-	0.081	0.350	-	-19.6	-	0.348
H65A	Is1	972	28/10/2014 23:11:06	-	0.29	0.339	-	-14.2	-	0.337
H65A	Is2	972	28/10/2014 23:12:45	-	0.19	0.328	-	-22.2	-	0.326
H65A	Is3	972	28/10/2014 23:14:39	-	0.31	0.315	-	-6.9	-	0.314
H65A	Is4	972	28/10/2014 23:16:30	-	0.32	0.300	-	35.0	-	0.303
H65A	Is5	972	28/10/2014 23:18:47	-	0.13	0.287	-	40.1	-	0.290
H65A	Iw	972	28/10/2014 23:09:23	-	0.37	0.351	-	-13.1	-	0.349
G64A	Is1	995	28/10/2014 23:12:31	-	0.099	0.334	-	8.9	-	0.335
G64A	Is2	995	28/10/2014 23:14:20	-	0.27	0.327	-	-31.3	-	0.323
G64A	Is3	995	28/10/2014 23:15:59	-	0.33	0.310	-	34.5	-	0.313
G64A	Is4	995	28/10/2014 23:17:51	-	0.59	0.300	-	29.1	-	0.302
G64A	Is5	995	28/10/2014 23:20:13	-	0.088	0.288	-	30.0	-	0.290
TIGA	It4	1027	28/10/2014 23:46:16	-	0.10	-	-	-	-	0.206
H66A	Is1	1030	28/10/2014 23:13:54	-	0.30	0.341	-	-37.8	-	0.337
H66A	Is2	1030	28/10/2014 23:15:35	-	0.18	0.322	-	43.4	-	0.326
H66A	Is3	1030	28/10/2014 23:17:23	-	0.27	0.316	-	0.4	-	0.316
H66A	Is4	1030	28/10/2014 23:19:07	-	0.49	0.310	-	-50.2	-	0.306
H66A	Is5	1030	28/10/2014 23:20:58	-	0.27	0.296	-	5.7	-	0.296
H66A	Iw	1030	28/10/2014 23:12:06	-	0.90	0.347	-	20.0	-	0.350
G65A	Is1	1050	28/10/2014 23:15:00	-	0.22	0.333	-	30.0	-	0.337
G65A	Is2	1050	28/10/2014 23:16:42	-	0.17	0.329	-	-32.2	-	0.326
G65A	Is3	1050	28/10/2014 23:18:38	-	0.30	0.313	-	12.9	-	0.315
G65A	Is4	1050	28/10/2014 23:20:27	-	0.34	0.309	-	-44.4	-	0.305
G65A	Is5	1050	28/10/2014 23:22:07	-	0.20	0.295	-	17.6	-	0.296
G65A	Is6	1050	28/10/2014 23:24:17	-	0.11	0.284	-	24.9	-	0.286
G65A	Iw	1050	28/10/2014 23:13:13	-	0.24	0.352	-	-30.4	-	0.349
I51GB	Is3	1153	28/10/2014 23:23:00	308.1	0.031	0.325	-1.1	-56.4	-1.9	0.320
I51GB	Is4	1153	28/10/2014 23:24:38	307.9	0.23	0.316	-1.4	-53.7	-1.5	0.312
I51GB	Is5	1153	28/10/2014 23:26:15	308.0	0.38	0.303	-1.6	11.2	-1.4	0.304
I51GB	Is6	1153	28/10/2014 23:28:03	308.1	0.56	0.293	-1.9	35.7	-1.2	0.295
I51GB	Is7	1153	28/10/2014 23:30:09	308.9	0.048	0.288	-2.3	-25.6	-1.6	0.286

References

Alcoverro B, Le Pichon A (2005) Design and optimization of a noise reduction system for infrasonic measurements using elements with low acoustic impedance. J Acoust Soc Am 117:1717–1727. https://doi.org/10.1121/1.1804966

Assink JD, Waxler R, Drob D (2012) On the sensitivity of infrasonic traveltimes in the equatorial region to the atmospheric tides. J Geophys Res 117:D01110. https://doi.org/10.1029/2011JD016107

Assink J, Smets P, Marcillo O, Weemstra C, Lalande J-M, Waxler R, Evers L (2019) Advances in infrasonic remote sensing methods. In: Le Pichon A, Blanc E, Hauchecorne A (eds) Infrasound monitoring for atmospheric studies, 2nd edn. Springer, Dordrecht, pp 605–632

Brachet N, Brown D, Le Bras R, Cansi Y, Mialle P, Coyne J (2009) Monitoring the Earth's atmosphere with the global IMS infrasound network. In: Le Pichon A, Blanc E, Hauchecorne A (ed) Infrasound monitoring for atmospheric studies. Springer, New York, pp 77–118. ISBN 978–1-4020-9508-5

Brown DJ et al (2002) Infrasonic signal detection and source location at the prototype international data center, pure and appl. Geophys. 159:1081–1125

Candel SM (1977) Numerical solution of conservation equations arising in linear wave theory: application to aeroacoustics. J Fluid Mech 83(3):465–493

Cansi Y (1995) An automatic seismic event processing for detection and location—the PMCC method. Geophys Res Lett 22(9):1021–1024

Ceranna L, Le Pichon A, Green DN, Mialle P (2009) The Buncefield explosion: a benchmark for infrasound analysis across central Europe. Geophys J Int 177:491–508

Che IY, Le Pichon A, Kim K, Shin IC (2017) Assessing the detection capability of a dense infrasound network in the southern Korean Peninsula. Geophys J Int 210:1105–1114. https://doi.org/10.1093/gji/ggx222

Chunchuzov I, Kulichkov S (2019) Internal gravity wave perturbations and their impacts on infrasound propagation in the atmosphere. In: Le Pichon A, Blanc E, Hauchecorne A Infrasound monitoring for atmospheric studies, 2nd edn. Springer, Dordrecht, pp 551–590

Cugnet D, de la Camara A, Lott F, Millet C, Ribstein B (2019) Non-orographic gravity waves: representation in climate models and effects on infrasound. In: Le Pichon A, Blanc E, Hauchecorne A (eds) Infrasound monitoring for atmospheric studies, 2nd edn. Springer, Dordrecht, pp 827–844

De Groot-Hedlin C, Hedlin M (2014) Infrasound detection of the Chelyabinsk meteor at the USArray. Earth Planet Sci Lett 402:337–345. https://doi.org/10.1016/j.epsl.2014.01.031

De Groot-Hedlin CD, Hedlin MAH (2015) A method for detecting and locating geophysical events using groups of arrays. Geophys J Int 203:960–971. https://doi.org/10.1093/gji/ggv345

De Groot-Hedlin CD (2017) Infrasound propagation in tropospheric ducts and acoustic shadow zones. J Acoust Soc Am 142:1816. https://doi.org/10.1121/1.5005889

de Groot-Hedlin C, Hedlin M (2019) Detection of infrasound signals and sources using a dense seismic network. In: Le Pichon A, Blanc E, Hauchecorne A (eds) Infrasound monitoring for atmospheric studies, 2nd edn. Springer, Dordrecht, pp 669–699

Drob DP, Picone JM, Garcés M (2003) Global morphology of infrasound propagation. J Geophys Res 108:4680. https://doi.org/10.1029/2002JD003307

Drob DP et al (2008) An empirical model of the Earth's horizontal wind fields: HWM07. J Geophys Res 113. https://doi.org/10.1029/2008ja013668

Drob DP, Broutman D, Hedlin MA, Winslow NW, Gibson RG (2013) A method for specifying atmospheric gravity wavefields for long-range infrasound propagation calculations. J Geophys Res Atmos 118:3933–3943. https://doi.org/10.1029/2012JD018077

Edwards WN, de Groot-Hedlin CD, Hedlin MAH (2014) Forensic investigation of a probable meteor sighting using USArray acoustic data. Seism Res Lett 85:1012–1018. https://doi.org/10.1785/0220140056

Evers LG, Haak HW (2007) Infrasonic forerunners: exceptionally fast acoustic phases. Geophys Res Lett 34:L10806. https://doi.org/10.1029/2007GL029353

Fee D et al (2013) Overview of the 2009 and 2011 Sayarim Infrasound calibration experiments. J Geophys Res Atmos 118:6122–6143. https://doi.org/10.1002/jgrd.50398

Gainville O, Blanc-Benon P, Blanc E, Roche R, Millet C, Le Piver F, Despres B, and Piserchia PF (2009) Misty picture: a unique experiment for the interpretation of the infrasound propagation from large explosive sources. In: Le Pichon A, Blanc E, Hauchecorne A (ed) infrasound monitoring for atmospheric studies. Springer, New York, pp 575–598. ISBN 978-1-4020-9508-5

Garcés MA, Hansen RA, Lindquist KG (1998) Traveltimes for infrasonic waves propagating in a stratified atmosphere. Geophys J Int 135:255–263

Garcés MA (2013) On infrasound standards, part 1: time, frequency, and energy scaling. InfraMatics 2:13–35. https://doi.org/10.4236/inframatics.2013.22002, http://www.scirp.org/journal/PaperInformation.aspx?PaperID=33802

Garces M (2019) Explosion source models. In: Le Pichon A, Blanc E, Hauchecorne A (eds) Infrasound monitoring for atmospheric studies, 2nd edn. Springer, Dordrecht, pp 273–345

Gardner CS, Hostetler CA, Franke SJ (1993) Gravity wave models for the horizontal wave number spectra of atmospheric velocity and density fluctuations. J Geophys Res 98(D1):1035–1049. https://doi.org/10.1029/92JD02051

Gibbons SJ et al (2015) The European Arctic: a laboratory for seismo-acoustic studies. Seism Soc Am 86:917–928. https://doi.org/10.1785/0220140230

Green D, Le Pichon A, Ceranna L, Evers L (2009) Ground truth events: Assessing the capability of infrasound networks using high resolution data analyses. In Le Pichon A, Blanc E, Hauchecorne A (ed) Infrasound monitoring for atmospheric studies. Springer, New York, pp 599–625. ISBN 978-1-4020-9508-5

Green D, Vergoz J, Gibson R, Le Pichon A, Ceranna L (2011) Infrasound radiated by the Gerdec and Chelopechene explosions: propagation along unexpected paths. J Int, Geophys. https://doi.org/10.1111/j.1365-246X.2011.04975.x

Kim K, Rodgers A (2016) Waveform inversion of acoustic waves for explosion yield estimation. Geophys Res Lett 43:6883–6890

Kinney G, Graham K (1985) Explosive Shocks in Air, 2nd edn. Springer, New York

Kulichkov SN (2009) On the prospects for acoustic sounding of the fine structure of the middle atmosphere. In Le Pichon A, Blanc E, Hauchecorne A (ed) Infrasound Monitoring for atmospheric studies. Springer, New York, pp 511–540. ISBN 978-1-4020-9508-5

Kulichkov SN, Chunchuzov IP, Popov OI (2010) Simulating the influence of an atmospheric fine inhomogeneous structure on long-range propagation of pulsed acoustic signals. Izv Russ Acad Sci Atmos Ocean Phys Engl Trans 46(1):60–68. https://doi.org/10.1134/s0001433810010093

Le Pichon A, Blanc E, Drob D (2005) Probing high-altitude winds using infrasound. J Geophys Res 110:D20104. https://doi.org/10.1029/2005JD006020

Le Pichon A, Ceranna L, Vergoz J (2012), Incorporating numerical modelling into estimates of the detection capability of the IMS infrasound network. J Geophys Res. https://doi.org/10.1029/2011jd0166702009

Le Pichon A, Ceranna L, Pilger C, Mialle P, Brown D, Herry P, Brachet N (2013) The 2013 Russian fireball largest ever detected by CTBTO infrasound sensors. Geophys Res Lett 40:3732–3737. https://doi.org/10.1002/grl.50619

Le Pichon A et al (2015) Comparison of co-located independent ground-based middle-atmospheric wind and temperature measurements with Numerical Weather Prediction models. J Geophys Res Atmos 120. https://doi.org/10.1002/2015jd023273

Lighthill MJ (1963) Jet Noise. AIAA J 1(7):1507–1517. https://doi.org/10.2514/3.1848

Marty J (2019) The IMS infrasound network: current status and technological developments. In: Le Pichon A, Blanc E, Hauchecorne A (eds) Infrasound monitoring for atmospheric studies, 2nd edn. Springer, Dordrecht, pp 3–62

Merchant BJ (2015) Hyperion 5113/GP infrasound sensor evaluation. Sandia Report SAND2015–7075, Sandia National Laboratories

Mialle P, Brown D, Arora N, colleagues from IDC (2019) Advances in operational processing at the international data centre. In: Le Pichon A, Blanc E, Hauchecorne A (eds) Infrasound monitoring for atmospheric studies, 2nd edn. Springer, Dordrecht, pp 209–248

Millet C, Robinet J-C, Roblin C (2007) On using computational aeroacoustics for long-range propagation of infrasounds in realistic atmospheres. Geophys Res Lett 34:L14814. https://doi.org/10.1029/2007GL029449

NASA (2015) Independent Review Team. Orb–3 Accident Investigation Report Executive Summary, Oct 9. https://www.nasa.gov/sites/default/files/atoms/files/orb3_irt_execsumm_0.pdf

Nippress A, Green DN, Marcillo OE, and Arrowsmith SJ (2014) Generating regional infrasound celerity-range models using ground-truth information and the implications for event location. Geophys J Int 197(2):1154–1165. https://doi.org/10.1029/2007GL029449

Picone JM et al (2002) NRL-MSISE-00 empirical model of the atmosphere: statistical comparisons and scientific issues. J Geophys Res 107. https://doi.org/10.1093/gji/ggu049

Pierce AD, Posey JW, Moo CA (1973) Generation and propagation of infrasonic waves, Air Force Cambridge Research Laboratories, Massachusetts Institute of Technology, Report AD-766472, 131 p

Pulli JJ, Kofford A (2015) Infrasound analysis of the October 28, 2014, Antares rocket failure at Wallops Island, Virginia, using video recordings as ground truth. J Acoust Soc Am 137. https://doi.org/10.1121/1.4920619

Raspet R, Abbott J-P, Webster J, Yu J, Talmadge C, Alberts II K, Collier S, Noble J (2019) New systems for wind noise reduction for infrasonic measurements. In: Le Pichon A, Blanc E, Hauchecorne A (eds) Infrasound monitoring for atmospheric studies, 2nd edn. Springer, Dordrecht, pp 91–124

Reed JW (1977) Atmospheric attenuation of explosion waves. J Acoust Soc Am 61:39–47

Sabatini R, Marsden O, Bailly C, Bogey C (2016) A numerical study of nonlinear infrasound propagation in a windy atmosphere. J Acoust Soc Am 140. https://doi.org/10.1121/1.4958998

Smart E, Flinn EA (1971) Fast frequency-Wavenumber analysis and Fisher signal detection in real time infrasonic array data processing. Geophys J Roy Astr Soc 26:279–284

Sutherland LC, Bass HE (2004) Atmospheric absorption in the atmosphere up to 160 km. J Acoust Soc Am 115(3):1012–1032, https://doi.org/10.1121/1.1631937

Talmadge C, Waxler R, Di X, Gilbert K, Kulichkov S (2008) Observation of low-frequency acoustic surface waves in the nocturnal boundary layer. J Acoust Soc Am 124. https://doi.org/10.1121/1.2967474

Varnier J (2001) Experimental study and simulation of rocket engine free jet noise. AIAA J 39 (10):1851–1859. https://doi.org/10.2514/2.1199

Virieux J, Garnier N, Blanc E, Dessa J-X (2004) Paraxial ray tracing for atmospheric wave propagation. Geophys Res Lett 31:L20106. https://doi.org/10.1029/2004GL020514

Walker KT, Hedlin M (2009) A review of wind-noise reduction methodologies. In: Le Pichon A, Blanc E, Hauchecorne A (eds) infrasound monitoring for atmospheric studies. Springer, New York, pp 141–182. ISBN 978-1-4020-9508-5

Walker KT, Shelby R, Hedlin MAH, deGroot-Hedlin C, Vernon F (2011) Western U.S. Infrasonic Catalog: Illuminating infrasonic hot spots with the USArray. J Geophys Res 116:B12305. https://doi.org/10.1029/2011jb008579

Waxler R, Evers L, Assink J, Blom P (2015) The stratospheric arrival pair in infrasound propagation. J Acoust Soc Am 137:4. https://doi.org/10.1121/1.4916718

Waxler R (2003) Modal expansions for sound propagation in the nocturnal boundary layer. J Acoust Soc Am 115. https://doi.org/10.1121/1.1646137

Waxler R, Assink J (2019) Propagation modeling through realistic atmosphere and benchmarking. In: Le Pichon A, Blanc E, Hauchecorne A (eds) Infrasound monitoring for atmospheric studies, 2nd edn. Springer, Dordrecht, pp 509–549

Whitaker RW, Sandoval TD, Mutschlecner JP (2003) Recent infrasound analysis. In: Proceedings of the 25th annual seismic research symposium in Tucson, AZ, pp 646–654